ICARUS 84, 118–153 (1990)

A Time-Dependent Dusty Gas Dynamic Model of Axisymmetric Cometary Jets

A. KÖRÖSMEZEY[1] AND T. I. GOMBOSI

Space Physics Research Laboratory, Department of Atmospheric, Oceanic and Space Sciences, University of Michigan, Ann Arbor, Michigan 48109

Received December 5, 1988, revised June 21, 1989

The first results of a new time-dependent, axisymmetric dusty gas dynamical model of inner cometary atmospheres are presented. The model solves the coupled, time-dependent continuity, momentum, and energy equations for a gas–dust mixture between the nucleus surface and 100 km using a 40 × 40 axisymmetric grid structure. The time-dependent multidimensional partial differential equation system was solved with a new numerical technique employing a second-order accurate Godunov-type scheme with dimensional splitting. It is found that narrow axisymmetric jets generate a subsolar dust spike and a jet cone, where a significant amount of the jet ejecta is accumulated. This subsolar dust spike has not been predicted on earlier calculations. The opening angle of the jet cone depends on the jet strength and it also varies during the time-dependent phase of the jet. For weak jets the steady-state half-opening angle is about 50°. In the case of the strong jets the jet cone extends to the nightside in good agreement with the Giotto imaging results.

1. INTRODUCTION

Our present, postencounter understanding of cometary nuclei is based on Whipple's (1950) "dirty iceball" idea, which visualizes them as chunks of ice, rock, and dust with negligible surface gravity. Whipple's hypothesis quickly replaced the century-long series of "sandbank" models, wherein the nucleus was thought of as a diffuse cloud of small particles traveling together. As comets approach the Sun, water vapor and other volatile gases sublimate from the surface layers, generating a rapidly expanding dusty atmosphere. The sublimated gas molecules (often called parent molecules) undergo collisions and various fast photochemical processes in the near nucleus region, thus producing a whole chain of daughter atoms and molecules. There is growing evidence that delayed gas emission from dust particles, dust grain photochemistry, as well as gas–dust chemical reactions also contribute to the maintenance of cometary atmospheres.

In the vicinity of the nucleus the gas and dust flows are strongly coupled: frequent gas–dust collisions accelerate small grains to velocities up to several hundreds of meters per second and inject them into the extensive cometary exosphere, where the gas and dust are decoupled. The expanding gas eventually converts most of its original internal energy to bulk motion, while it also loses momentum and energy to the dust flow.

It was recognized as early as the mid-1930s that gas outflow plays an important role in cometary dust production. In early treatments of the gas–dust interaction it was assumed that the gas drag coefficient was independent of the gas parameters and that the gas velocity was constant in the dust acceleration region. In the late 1960s this very naive picture was replaced by a

[1] Permanent address: Central Research Institute for Physics, Hungarian Academy of Sciences, Budapest, Hungary.

0019-1035/90 $3.00

two-component approach, which used free molecular approximation to describe the rarefield gas flow and neglected the random motion of the dust particles. In Probstein's (1968) dusty gas dynamic treatment (which later became the prototype of such calculations), the traditional gas energy conservation equation was replaced by a combined dust–gas energy integral. This approach was later considerably refined by a series of authors (Shulman 1972, Hellmich and Keller 1980, Gombosi *et al.* 1983, 1985, Marconi and Mendis 1982, 1983, 1984, 1986, Kitamura 1986, 1987), but it still represents the main method of dusty gas dynamics calculations.

Modeling efforts have shown that the spatial extent of the dust acceleration region (where dust particles accelerate to about 80% of their terminal velocity) is less than about 30 cometary radii. Gas particles typically spend less than 10^2 sec in this region, which is not long enough for any significant change in the gross chemical composition of the gas. In a first approximation a single-fluid dusty gas hydrodynamical technique seems to be adequate for describing the overall dynamics of the gas–dust interaction.

The Comet Halley imaging experiments showed that cometary activity is concentrated to limited areas on the sunlit side of the nucleus, with most of the dust ejection coming from fairly localized jets. These results underscored the necessity for multidimensional dusty gas flow models, which can describe the highly anisotropic gas and dust flows in the inner cometary coma. Following an axisymmetric pure gas cometary coma model (Vergazov and Krasnobaev 1985) the first multidimensional dusty gas model was published by Kitamura (1986), who developed a time-dependent 2D dusty gas dynamic code using one characteristic dust size, simple energetics, and a highly simplified chemistry (in what follows, this paper will be referred to as K'86). In a follow-up paper Kitamura (1987) also investigated the multidimensional dynamics of isolated jets (when all the gas and dust are produced by a limited active region), as well as the viscous flow of pure gas jets (this paper will be referred to as K'87). In the isolated jet calculation published in K'87 no background gas ejection was assumed, and therefore the nightside gas became too tenuous to be described by inviscid hydrodynamic equations. On the basis of this consideration the K'87 model did not solve the gas and dust transport equations beyond the terminator in the case of isolated dusty jets. In these two papers Kitamura (1986, 1987) concentrated on the study of steady-state solutions, because he thought they were the first important step toward better understanding of cometary jet-related phenomena. However, in the light of the latest Giotto imaging results it seems to be important to extend the models to the nightside, as well.

The pioneering work of Kitamura (1986, 1987) represented the first step toward the modeling of multidimensional dusty gas dynamic phenomena in the collision-dominated inner region of dusty cometary atmospheres. Even though Kitamura has applied several numerical techniques (such as MacCormack's explicit method, several first- and second-order upwind differencing methods, and an implicit method) it seems to be useful to develop other independent multidimensional dusty jet models. The K'86 and K'87 models concentrate on the steady-state features of the nonspherically symmetric dusty gas flow and do not study time-dependent phenomena. Therefore one of the natural next steps is to study the time-dependent behavior of the dusty jet evolution. Also, Kitamura investigated only some fundamental physical scenarios, such as the case of a very weak jet on top of isotropic background, and the case of isolated jets (with and without background gas emission), when all dust production is concentrated in a limited active area. Naturally, there are a large number of other physically interesting and relevant cases, which can be investigated by independent

multidimensional models. An independent multidimensional dusty gas dynamic model is also useful from the point of view of minimizing potential human error in implementing these complicated numerical models.

Our long-term goal is to develop a multidimensional, dusty gas dynamics model which is capable of describing transient phenomena, such as sudden outbursts, propagation, and evolution of shocks, etc. As a first step toward this goal we developed an axially symmetric model describing the coupled flow of an inviscid single species (H_2O) gas and nonvolatile dust particles. Even though the mathematical formulation and the implemented computer code allows the use of several dust sizes, in the first application we considered only one characteristic dust size (0.65 μm). This simplification greatly reduced the run time of code, which was an important consideration. The use of inviscid gas equations restricts the validity of our model to collision-dominated (relatively dense) situations. The physical models considered in this paper satisfy this condition (in the near nucleus region the mean free path of molecular collisions is less than a few meters even on the night side). It is interesting to note that Kitamura (1987) has considered very low density viscous gas flows in the pure gas jet case. In the K'87 paper he makes the statement that "the dominance of the viscosity terms near the surface made the convergence of the solution very difficult for the rarefield gas jets." The development of viscous dusty gas flow models of cometary jets is eventually very desirable, but at this point the much simpler to implement inviscid models can also make valuable contributions to our understanding of physical processes in inner cometary comae.

Another important assumption used by the present generation of multidimensional cometary jet models is the conservation of dust particles in the coma. This means that the dust grains are neither created nor destroyed (or fragmented) in the gas–dust interaction region, and no additional sublimation or recondensation is considered in this region. There is growing indication that these assumptions are not necessarily true and the next generation of cometary jet models must address this question. One potentially important effect to be considered is the recondensation of gas in the near nucleus region, where strong adiabatic cooling reduces the gas temperature well below 100°K. It is possible that this recondensation process is capable of modifying the jet structure. Also, radiative transfer (and its potential consequences to the gas and dust heating rates) is not considered by the present models.

Some of the numerical methods used by Kitamura to describe pure gas jets (specifically the first- and second-order accurate upwind differencing schemes) are quite capable of describing discontinuous dusty gas flows. On the other hand the dusty jet calculations were carried out with MacCormack's method in the K'86 model and with a first-order upwind differencing scheme in the K'87 model. Kitamura used the more accurate Godunov-type schemes (such as the second-order upwind differencing scheme recommended by van Albada *et al.* (1982)) only to describe pure gas jets. In this paper we implement a second-order accurate Godunov-type scheme with dimensional splitting, which is a modified version of the van Albada *et al.* (1982) method. Our modified method (which was developed with the help of Dr. Bram van Leer, who is a coauthor of the van Albada *et al.* (1982) paper) is especially tuned for describing strong shocks and discontinuities. The numerical scheme itself is fast, relatively easy to implement, and has second-order accuracy in both space and time. As has been discussed by van Albada *et al.* (1982), this type of method is very suitable for astrophysical gas dynamic calculations.

This paper presents detailed results obtained with our new, time-dependent, two-dimensional (axisymmetric) dusty jet model. The model solves the coupled, time-dependent continuity, momentum, and en-

ergy equations for an inviscid dust–gas mixture. A very low pressure external "vacuum cleaner" was placed at a distance of 100 km, which helped to ensure a supersonic flow in most of the integration region. A 40 × 40 grid structure was employed in the integration region. There were 40 linearly spaced azimuthal and 40 logarithmically spaced radial grids extending from 6 to 100 km. The time-dependent, coupled multidimensional partial differential equation system was solved with a second-order accurate Godunov-type scheme with dimensional splitting.

2. EARLIER 2D DUSTY JET CALCULATIONS

The first nonspherically symmetric model of inner cometary atmospheres was published by Kitamura in 1986 (K'86). In this paper Kitamura described relatively weak, Giacobini–Zinner class comets (the adopted gas production rate was about 10^{29} molecules sec^{-1}) with a dust to gas mass production rate ratio of $\chi = 1$. In this section we discuss only the dusty gas dynamic results of the K'86 model, which considered the effects of a narrow (half opening angle about 10°) dusty gas jet. The contribution of this narrow jet to the total production rate was small ($Q_{jet}/Q_{total} \approx 0.07$). It is assumed that at the surface the velocity of the outflowing gas is the local sound velocity and the mass density of the gas is given by

$$\rho(\Theta) = \rho_0 \left[(\alpha - 1) \exp\left(-\frac{\Theta^2}{\Theta_0^2} \right) + 1 \right], \quad (1)$$

where $\rho_0 = 2.5 \times 10^{12}$ m(H_2O) g/cm^3, $\alpha = 10$, and $\Theta_0 = 10°$. The outflowing gas temperature at the surface was chosen to be the same as the sublimation temperature, $T_s = 200$°K. It was recently extensively discussed by Crifo (1988) that the temperature of the nearly supersonically outflowing gas must be considerably smaller than the sublimation temperature, because the internal energy of the sublimating gas is the source of both the bulk and the random energies of the outflowing gas. By keeping the temperature of the outflowing gas at the sublimation temperature, the K'86 model (and the K'87 model as well) overestimates the energy and momentum available for the gas and dust acceleration.

Figure 1 shows steady-state gas and dust density distributions obtained with the axially symmetric K'86 model. Inspection of Fig. 1 reveals that the originally 10°-wide active region eventually produces a much broader jet (the effective half-opening angle is about 35°). The physical reason for this broadening is that the horizontal pressure gradient generates a lateral gas flow, which in turn accelerates the dust grains in the horizontal direction, too. This process in effect "sweeps out" most of the grains from the subsolar region, i.e., from the region above the active region. The horizontal expansion represents an additional expansion direction for the gas released from the active region; therefore, the pressure of this gas component decreases faster than that of the background gas. Kitamura concluded that at some point a pressure balance is reached between the background gas and the jet ejecta, and this balance eventually stops the horizontal gas expansion. This means that there will be a dust accumulation near the pressure balance surface, which in this case happens to be a conical surface with a half-opening angle of about 35°. Kitamura's result is very interesting: it indicates that weak jets may eventually cause a dust density decrease above the active area and that the dust accumulation is concentrated on a conical surface much beyond the angular extent of the jet itself.

In a follow-up paper (K'87), Kitamura investigated the case of isolated jets, i.e., when all dust production is concentrated to a localized subsolar active area. Inside the active area the gas production was assumed to be isotropic with a dust to gas mass production rate ratio of $\chi = 0.2$, while no dust was produced outside of the jet. However, when Kitamura considered a dusty gas jet with a uniform gas production background,

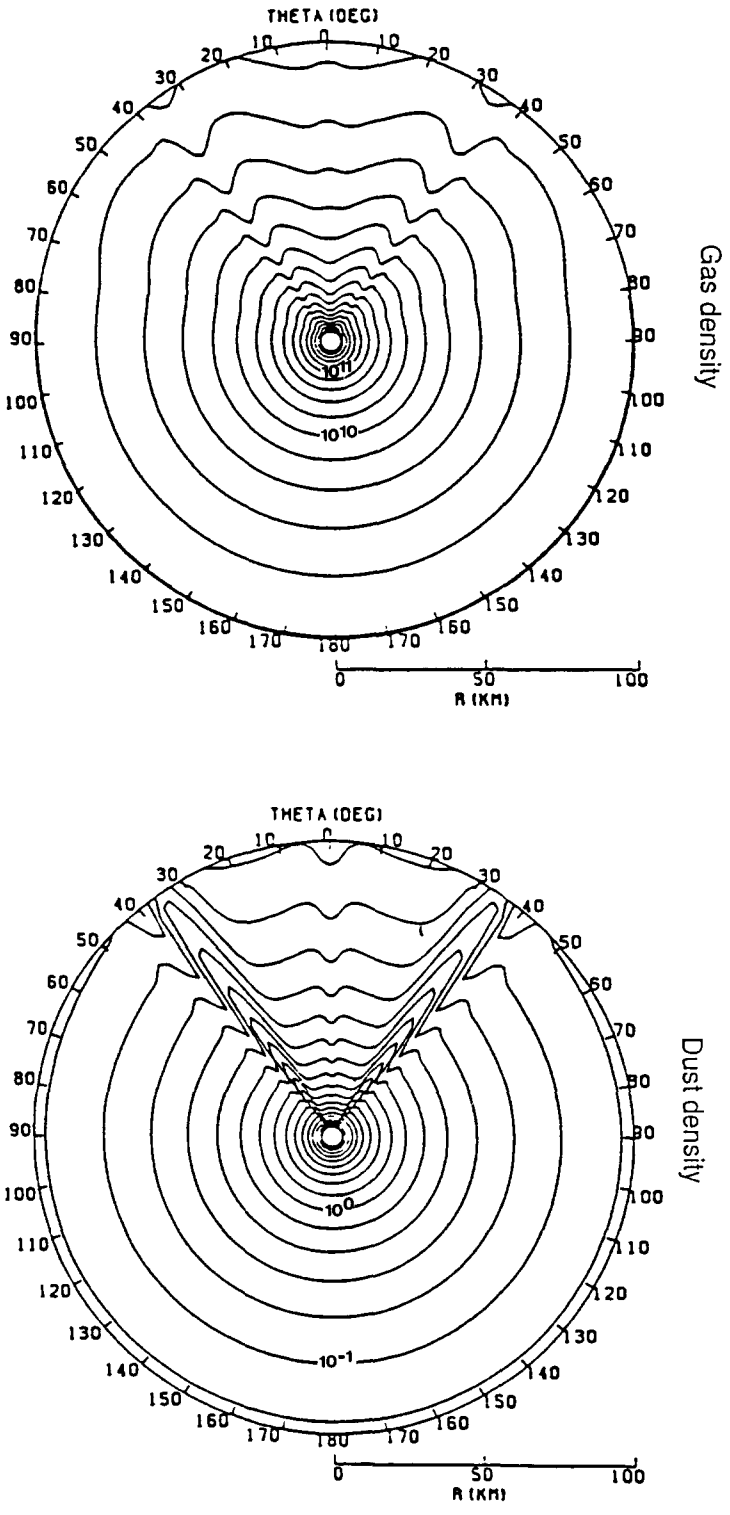

FIG. 1. Gas and dust isodensity contours in the inner cometary coma. The nucleus is modeled as an isotropic background source of gas and dust with a narrow subsolar active region. The jet/background production rate ratio is 0.07 (from Kitamura 1986)

this assumption resulted in a very low dust/gas mass ratio. In this paper the governing equations were solved only for the dayside (with a low-pressure external boundary at $\Theta = 90°$), because the inviscid flow equations were not valid in the nightside region, where the gas density was very low. At the nuclear surface outside the active area the K'87 model adopted slip flow conditions to describe the interaction of the gas flow with the nucleus.

In the same paper, Kitamura (1987) also investigated an alternative scenario. In this case the gas production was assumed to be uniform all over the nucleus (no cross-terminator flow), while the dust production was concentrated to a limited subsolar area. Figure 2 shows the appropriate gas and dust density distributions obtained with the K'87 model. It is obvious from the description of the physical problem that when uniform surface gas production is assumed horizontal gas pressure gradients will develop only as a result of the dust mass loading; therefore one can only expect moderate horizontal gas and dust transport. Inspection of Fig. 2 shows that this is really the case. One can clearly see the effects of the gas–dust interaction in the subsolar region. One could say that this solution is essentially a combination of a spherically symmetric radial dusty gas flow in the subsolar region and a pure spherically symmetric radial gas flow elsewhere (Table I).

Very recently Gombosi and Korosmezey developed a new 2D, time-dependent, axisymmetric dusty gas dynamic jet model (Gombosi and Körosmezey 1988a,b). The model solves the coupled, time-dependent continuity, momentum, and energy equations for an inviscid dust–gas mixture (described in detail in the next section). Gombosi and Körosmezey (1988a) were able to reproduce the narrow dusty jet case of the K'86 model. For the sake of benchmarking the results against the K'86 model, Gombosi and Körosmezey (1988a) considered a narrow jet with an outflow gas temperature of 200°K (however, as it was discussed above this assumption lead to an overestimate of the gas and dust acceleration in the inner coma). In this paper we present several alternative physical scenarios, which predict the possibility of some additional gas and dust features in the inner commetary coma, which were not seen in earlier calculations.

3 MODEL

The physical model considered in this paper describes an interacting mixture of expanding cometary gas and nonvolatile dust grains. The gas component is assumed to be a nonviscid, compressible perfect fluid, while the gas–dust interaction is described using the free molecular approximation. These approximations naturally limit the potential physical scenarios to relatively active comets with distributed gas production rates. The free-molecular assumption

TABLE I

COMPARISON OF AXISYMMETRIC DUSTY JET MODELS

Narrow dusty jet case of K'86	Isolated dusty jet case of K'87	Present model
1 dust size	3 dust sizes	1 dust size
Uniform background emission	No background emission	Axisymmetric background emission
Weak jet ($Q_{jet}/Q_{background} \sim 0.07$)	Strong jet (isolated dust jet)	Strong jet ($Q_{jet}/Q_{background} \sim 0.6$)
G–Z class comet ($Q \sim 10^{29}$ sec^{-1})	Halley class comet ($Q \sim 10^{30}$ sec^{-1})	Halley class comet ($Q \sim 10^{30}$ sec^{-1})
$\chi = 1$	$\chi = 0.2$	$\chi = 0.3$
Subsolar jet	Subsolar jet	Subsolar jet
Steady-state results	Steady-state results	Time-dependent results
Day and night flow	Day flow only	Day and night flow
Vacuum at $r = 100$ km	Vacuum at $r = 100$ km and terminator	Vacuum at $r = 100$ km

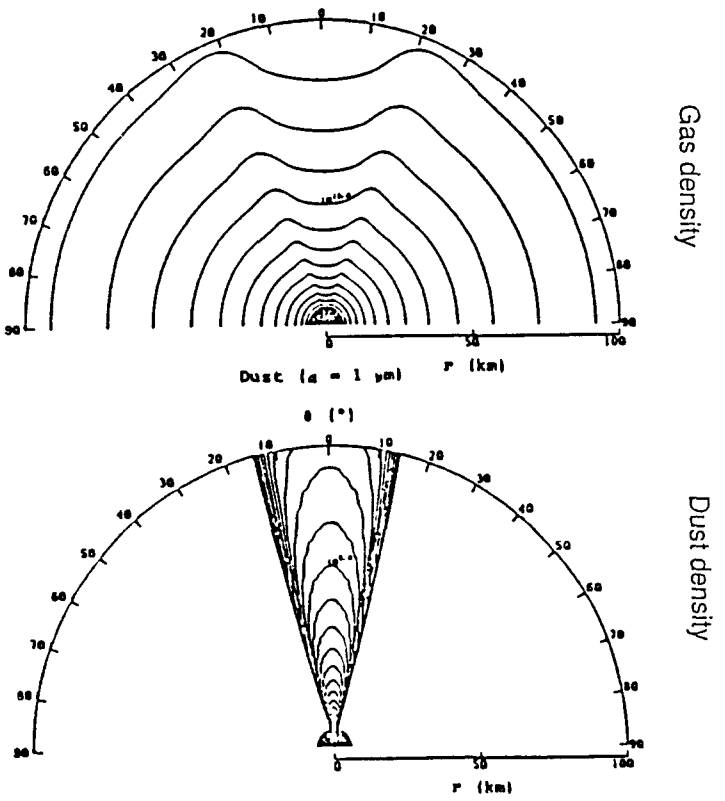

FIG. 2 Gas and dust isodensity contours in the inner cometary coma in the gas of an isolated dust jet. The nucleus is considered to be a uniform source of cometary gas, while dust production is concentrated to a narrow subsolar active region only (from Kitamura 1987)

(that the mean free path of molecular collisions is much larger than the grain size) is easily satisfied on most comets. For instance, the mean free path at the surface of Comet Halley is on the order of a meter or so. On the other hand, the gas concentration must be relatively high to justify the use of inviscid gas flow models. In a reasonably good approximation the mean free path of molecular collisions is $\lambda \approx 2 \times 10^{-4}/z$ (Crifo 1989), where λ is measured in units of centimeters, and the cometary gas mass production rate, z, is given in [g cm^{-2} sec^{-1}]. At the active regions of Comet Halley the production rate is about $z \approx 10^{-5}$ g · cm^{-2} · s^{-1}, so $\lambda \approx 0.2$ m. The mean free path at the surface of the much less active Giacobini–Zinner was at around 10 m, which is still small compared to the characteristic scale of the flow. The inviscid approximation essentially loses validity when one considers surface region with negligible gas production. In this paper we assume significant variations in the surface gas production rates, but the molecular mean free path everywhere remains much smaller than the characteristic scale of the gas flow.

As the vaporized gases leave the surface they drag away some of those dust grains which have already been evacuated of their ice component. The gas drag force accelerates the dust particles to terminal velocities comparable with the gas flow velocity. The mass, momentum, and energy conservation equations of the single-fluid, inviscid, perfect gas are

$$\frac{D\rho}{Dt} + \rho \nabla \cdot \mathbf{u} = 0 \tag{2}$$

$$\rho \frac{D\mathbf{u}}{Dt} + \nabla p - \rho \mathbf{g}_c = \mathbf{F}_{gd} \tag{3}$$

$$\frac{1}{\gamma - 1}\frac{Dp}{Dt} + \frac{\gamma}{\gamma - 1} p \nabla \cdot \mathbf{u} = Q_{ext} - Q_{gd}, \tag{4}$$

where

$$\frac{D}{Dt} = \frac{\partial}{\partial t} + (\mathbf{u} \cdot \nabla) \tag{5}$$

is the convective derivative, ρ = gas mass density, p = gas pressure, $\mathbf{u}$ = gas velocity, $\mathbf{g}_c$ = acceleration due to the gravitational attraction of the comet, $\mathbf{F}_{gd}$ = gas to dust momentum transfer rate, γ = gas specific heat ratio (in the present model a $\gamma = 4/3$ value was used, characterizing H_2O molecules), Q_{gd} = gas to dust energy transfer rate, and Q_{ext} = external heating rate. In the innermost coma where most of the gas–dust interaction takes place the radiation pressure effect and cometary gravity can be neglected and the equation of motion of an individual dust grain becomes

$$\frac{D_a \mathbf{V}_a}{Dt} = \frac{3}{4a\rho_a} p C'_D \mathbf{S}_a, \tag{6}$$

where

$$\frac{D_a}{Dt} = \frac{\partial}{\partial t} + (\mathbf{V}_a \cdot \nabla),$$

while $\mathbf{V}_a$ = dust particle velocity, a = dust radius, and ρ_a = dust bulk density. The dimensionless gas–dust relative velocity, s_a, and the modified free molecular drag coefficient, $C'_D = s_a C_D$ (where C_D is the free molecular drag coefficient for a perfect sphere), are (cf. Gombosi *et al.* 1986, Kitamura 1986)

$$\mathbf{s}_a = \frac{\mathbf{u} - \mathbf{V}_a}{\sqrt{2\frac{k}{m}T}} \tag{7}$$

$$C'_D = \frac{2\sqrt{\pi}}{3}\sqrt{\frac{T_a}{T}} + \frac{2s_a^2 + 1}{s_a^2\sqrt{\pi}} e^{-s_a^2} + \frac{4s_a^4 + 4s_a^2 - 1}{2s_a^3}\,\mathrm{erf}(s_a), \tag{8}$$

where s_a = magnitude of the normalized gas–dust relative velocity vector, while T and T_a are the gas and dust temperatures, respectively. In the presence of an external radiation field the energy balance equation for a single dust particle is (cf. Gombosi *et al.* 1986, Kitamura 1986)

$$C_a \frac{D_a T_a}{Dt} = \frac{3}{a\rho_a}\left[pC_H\sqrt{T} + \frac{1 - A_{VIS}}{4} I_{rad} - (1 - A_{IR})\sigma T_a^4\right], \tag{9}$$

where C_a = dust specific heat, A_{VIS} and A_{IR} are the visible and infrared dust albedos, respectively, while σ = Stefan–Boltzmann constant, and I_{rad} = radiation energy flux reaching the dust grain.

$$C_H = \frac{\Gamma_a}{8(\gamma - 1)}\sqrt{2\frac{k}{m}}\left[2\gamma + 2(\gamma - 1)s_a^2 - \frac{(\gamma - 1)\,\mathrm{erf}(s_a)}{4s_a\Gamma_a} - (\gamma + 1)\frac{T_a}{T}\right], \tag{10}$$

where

$$\Gamma_a = \frac{e^{-s_a^2}}{\sqrt{\pi}} + \left(\frac{1}{2s_a} + s_a\right)\mathrm{erf}(s_a). \tag{11}$$

Finally, it is assumed that the dust particles do not undergo any further sublimation or fragmentation in the coma (there is recent indication that this assumption is probably violated to some extent); consequently the dust size distribution function, f_a, must obey the following continuity equation:

$$\frac{D_a f_a}{Dt} + f_a \nabla \cdot \mathbf{V}_a = 0. \tag{12}$$

The gas to dust momentum and energy transfer rates can be obtained by integrating over all dust sizes:

$$F_{gd} = \pi p \int_0^{a_{max}} da\, C'_D a^2 f_a \mathbf{s}_a \tag{13}$$

$$Q_{gd} = \pi p \int_0^{a_{max}} da\, a^2 f_a (C'_D \mathbf{V}_a \cdot \mathbf{s}_a + C_H\sqrt{T}). \tag{14}$$

It should be noted that these integrals are dominated by the momentum and energy transfer to small particles. All calculations

presented in this paper were carried out with one characteristic dust size only; however, the formulation (and the numerical code) is capable of describing several sizes. External gas heating is caused mainly by photochemical and radiative heating/cooling processes (cf. Gombosi *et al.*, 1986), $Q_{ext} = Q_{phc} + Q_{IR}$. In a dense inner cometary coma the optical thickness effects are approximately compensated by focusing due to multiple scattering (cf. Mendis *et al.* 1985); therefore the photochemical heating rate can be approximated by the heating generated by the photodissociation of the dominant water molecules (cf. Mendis *et al.* 1985),

$$Q_{phc} = Q_0 \frac{n}{d^2}, \tag{15}$$

where the gas concentration can be written as $n = \rho/m$ (m being the mass of the gas molecules), while $Q_0 = 2.8 \times 10^{-17}$ erg cm^{-3} sec^{-1}, d = heliocentric distance (measured in AU). This value is in reasonably good agreement with the latest laboratory data (cf. Crifo 1988). At present, there is significant confusion regarding the infrared heating and cooling terms (cf. Crifo 1988); therefore these terms were neglected in the present calculation.

4 RESULTS

4.1. Parameter Values and Boundary Conditions

The present model considers a pure vapor inner atmosphere with $\gamma = 4/3$ and $m = 18m_p$ (where m_p is the atomic mass unit). All dust particles in the coma are assumed to have the same radius ($a = 0.65$ μm) and bulk density ($\rho_a = 1$ g cm^{-3}); consequently the mass of dust grains is uniformly $m_a = 1.15 \times 10^{-12}$ g. The dust specific heat was taken to be $C_a = 6 \times 10^6$ erg g^{-1} °K^{-1} (Kitamura 1986). The dust particles were assumed to be fluffy and very dark with visible and infrared albedos of $A_{VIS} = A_{IR} = 0.03$. All model calculations shown in this paper were carried out for a heliocentric distance of 0.9 AU; therefore the unattenuated solar radiation energy density was $I_{rad} = 1.35 \times 10^6/0.9^2 = 1.67 \times 10^6$ erg cm^{-2} sec^{-1}.

The coupled, time-dependent, axisymmetric continuity, momentum, and energy equations for the dust–gas mixture were solved using a second-order accurate Godunov-type scheme with dimensional splitting. This numerical scheme is a modified version of the technique developed by van Albada *et al.* (1982) and is especially tuned to describe the evolution of sharp shocks and discontinuities. A detailed description of the numerical method is given in the Appendix. The governing equations were solved on a 40 × 40 mesh. A linearly spaced grid structure was adopted in the azimuthal direction (extending from 0 to 180°), while in the radial direction the step size varied with cometocentric distance. In order to be able to resolve the transonic region with appropriate detail, the immediate vicinity of the nucleus (between 6 and 6.4 km) was divided into 10 logarithmically spaced intervals. The second region (characterized by supersonic gas flow), which extended from 6.4 to 100 km, contained 30 logarithmically spaced grid points. During the calculation, variable time steps were applied in both regions under the condition that the Courant number always had to be less than 0.9.

In the present model the nucleus–coma interface was not modeled self-consistently. It was assumed that the sublimation temperature was uniformly $T_{subl} = 200$°K, but the mantle thickness and its physical structure were not specified. Instead of specifying the mantle structure and solving the self-consistent outflow problem, the sublimation process was substituted by a reservoir containing stationary perfect gas at a temperature of $T = T_{subl}$ and a prescribed density. The gas mass density in the reservoir (assuming water vapor molecules) was approximated as the sum of two terms,

$$\rho(R_N, \Theta, t) = \rho_{jet}(\Theta, t) + \rho_{bckg}(\Theta, t), \tag{16}$$

where ρ_{bckg} is the background source com-

ing from the nonactive areas of the nucleus, while ρ_{jet} describes the jet source in the subsolar active region

$$\rho_{\text{jet}} = \rho_0 \, \alpha \exp\left(-\frac{\Theta^2}{\Theta_0^2}\right). \qquad (17)$$

In the present set of calculations our primary goal is to model narrow axisymmetric jets; therefore a $\Theta_0 = 10°$ value was adopted. Such a narrow jet can be generated, for instance, by a relatively fresh surface crack. The jet strength parameter, α, was a free parameter of the model. In this paper $\alpha = 15$ (weak jet) and $\alpha = 75$ (strong jet) values were used.

The surface temperature of the nucleus might be considerably higher than the sublimation temperature, mainly because the mantle is a good insulator. This surface temperature is "inherited" by the freshly emitted dust particles. In the present model a surface dust temperature value of 418°K was adopted, which is somewhat larger than the value used in the K'86 and K'87 models ($T_a = 348$°K). The reason for this discrepancy is that in the present work the light absorption efficiency of magnetite was adopted, which is higher than the corresponding value adopted by Kitamura (1986).

It was assumed that initially ($t = 0$) the near nucleus region was dust-free and filled with radially expanding low-density gas. At $t = 0$ an active area was generated on the surface of the spherical nucleus ($R_N = 6$ km). The gas and dust outflows were calculated in every time step using the reservoir outflow boundary condition described above. This model satisfies the energy conservation requirement at the surface (cf. Crifo 1988) and offers a reasonable treatment of the nucleus–coma interface, resulting in a standing hydrodynamic shock wave (with appropriate jump conditions) between the hypothetical gas reservoir and the first cell. A natural consequence of this boundary condition is that the flow is subsonic near the surface (as a result of the dust loading) and has a sonic transition in the inner coma (typically at a few tens of meters from the nucleus). Naturally, this boundary condition is one of the several possible treatments of the nucleus–coma interface. An alternative method was used by Kitamura (1986, 1987), who described the gas flow at the inner boundary assuming a prescribed gas density just above the surface and assuming sonic outflow velocity. The physical difference between the present model and Kitamura's boundary condition is that in the K'86 and K'87 models the outflowing gas had a different total energy content, because the bulk velocity of the outflowing gas was the sonic velocity corresponding to $T_s = 200$°K and the temperature of the gas itself was T_s as well.

Just above the surface (in the very first spatial cell) the dust velocity is still very small; therefore a large number of dust particles are present. These dust particles still "remember" the surface temperature, because they did not have enough time to reach a new equilibrium temperature. It is assumed that when these hot grains interact with the gas molecules in a free molecular manner the reflected gas molecules fully accommodate to the grain temperature. This process represents a considerable extra source of gas energy inside the active region, where the dust production rate is large. As a consequence of this interaction the outflowing gas temperature is a strong function of the solar zenith angle. For instance, in the case of the strong jet (to be discussed later) the subsolar outflow temperature is about 360°K (the surface temperature is 418°K), while at the antisolar point, where there is no direct sunlight and the gas production rate reaches its minimum value, the outflowing gas temperature is only about 130°K. The present boundary conditions represent a complicated set of time-dependent equations. Table II illustrates the resulting steady-state inner boundary conditions for the case of the strong dusty jet (to be discussed later). Table II shows the gas and dust parameters at

TABLE II

SOME STEADY-STATE GAS AND DUST PARAMETER VALUES NEAR THE NUCLEUS–COMA INTERFACE FOR THE STRONG DUSTY JET CASE

Θ (°)	u_r (km/sec)	n (cm^{-3})	$T(K)$	n_a (cm^{-3})	V_{ar} (km/sec)
2 25	0 208	$1\,8 \times 10^{15}$	363 7	$1\,5 \times 10^{4}$	0 212
11.25	0.204	$1\,3 \times 10^{15}$	343 3	$1\,0 \times 10^{4}$	0 194
20 25	0.165	$2\,6 \times 10^{14}$	237 1	$1\,9 \times 10^{3}$	0 145
47 25	0 187	$3\,2 \times 10^{13}$	162 1	$4\,0 \times 10^{2}$	0.108
83 25	0.210	$7\,0 \times 10^{12}$	147 1	1.5×10^{2}	0 079
110 25	0 226	$4\,2 \times 10^{12}$	138 0	$1\,2 \times 10^{2}$	0 072
137.25	0 227	$4\,2 \times 10^{12}$	134 6	$1\,2 \times 10^{2}$	0 072
173 25	0 230	$4\,2 \times 10^{12}$	127 8	$1\,2 \times 10^{2}$	0 072

Note The columns present the zenith angle, radial gas velocity, gas concentrations, gas temperature, dust number density, and radial dust velocity

a distance of 19 m above the surface of the nucleus.

At the beginning of the calculation the jet density was increased to full strength with an e-folding time scale of 100 sec. A very low pressure external medium was placed at a distance of 100 km, which helped to ensure a supersonic flow in most of the integration region.

4.2. Weak Jet with Isotropic Background

In an earlier paper we benchmarked our model with the K'86 model using the same outflow temperatures for both the gas and dust components. The results were very close to the results of the K'86 model (Gombosi and Körösmezey 1988a). In order to compare our present dusty jet model (which uses different inner boundary conditions than the earlier benchmark calculation) to the K'86 model we first considered a physical situation similar to Kitamura's (1986) narrow axisymmetric dusty jet. In this calculation a jet strength parameter value of $\alpha = 15$ was adopted, resulting in a somewhat stronger dusty jet (with respect to the background) than the one studied by Kitamura (1986). This jet was still weak enough to reproduce the main features of Kitamura's (1986) calculation. In our case about 11% of the total gas and dust production was concentrated inside the subsolar active region, as opposed to 7% in Kitamura's (1986) model. In order to generate a uniform background of gas and dust production, the background gas density in the sublimation reservoir, ρ_{bckg}, was assumed to be independent of the zenith angle, Θ. In this calculation a constant reservoir gas density value of $\rho_{bckg} = 2.5 \times 10^{-9}$ g/cm^3 was employed everywhere. The above model parameters describe a Halley-class comet with a total gas production rate of 2.1×10^{30} molecules sec^{-1} and dust to gas mass production rate ratio of 0.3. This is a much more active comet than the one used in K'86, which had about a factor of 20 smaller gas production. On the other hand the main features of the dust jet are fundamentally controlled by the jet/background production rate ratio, and this parameter was very close to the value used by K'86.

Figure 3 shows snapshots of the gas pressure, mass density, temperature, and radial velocity as well as the dust mass density and radial velocity distributions in the inner coma following the onset of a weak dusty jet superimposed on an isotropic background production. The results are shown in a cylindrical coordinate system: the horizontal axis in each panel shows the distance from the center of the comet along the Sun–comet line, while the vertical axis refers to the distance from the Sun–comet line. The Sun is always to the left in each panel. The jet is located in the subsolar region; therefore the Sun–comet line is an axis of symmetry of the solution. The solid lines represent the intersections of constant pressure, density, or velocity surfaces with the ecliptic plane.

One of the most striking features seen in Fig. 3 is the nearly radial expansion during the early phase of the jet. Initially the newly ejected gas and dust expands practically radially with relatively little horizontal transport. The main reason for this almost entirely radial outflow pattern is that the radial pressure gradient near the surface is much larger than the azimuthal gradient.

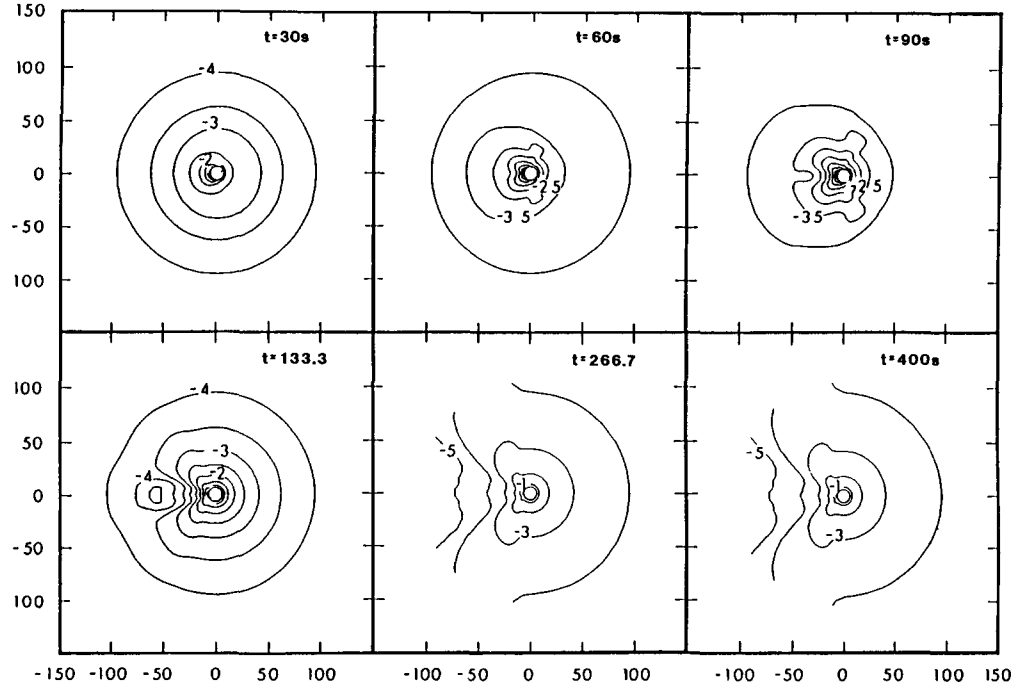

FIG. 3a. Snapshots of constant gas pressure contours following the onset of a weak jet at $t = 0$, superimposed on an isotropic background. The panels show contour plots of the 10-based logarithm of the gas pressure at t = 30, 60, 90, 133 3, 266.7, and 400 sec In each panel the axis of symmetry is a horizontal line going through the center. The sunward direction is to the left of each panel. All distances are given in kilometers.

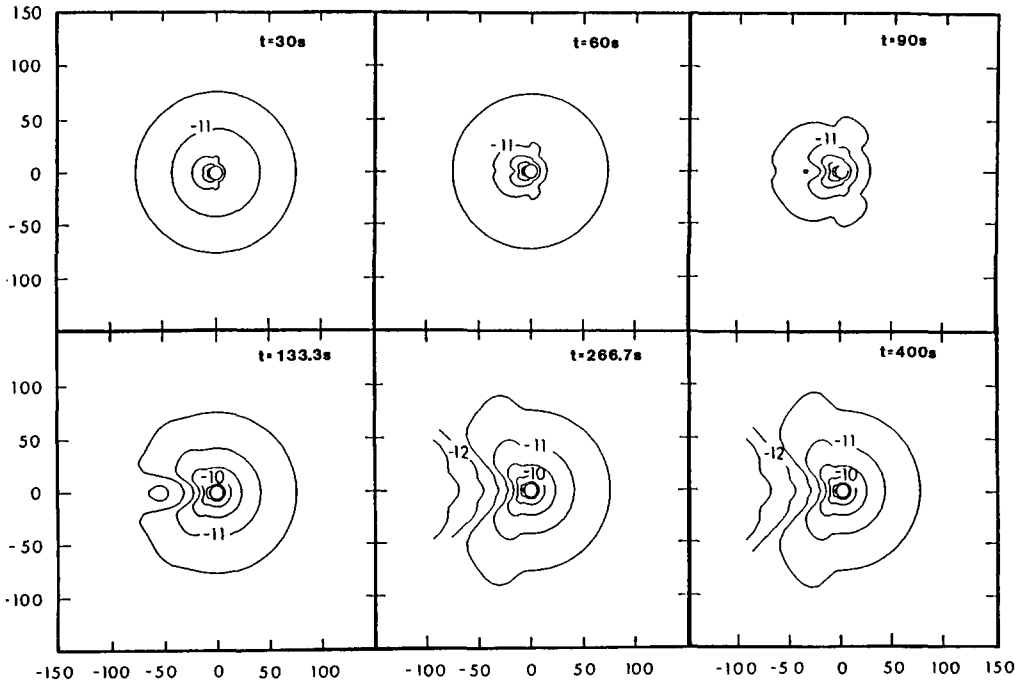

FIG. 3b. Snapshots of constant gas mass density contours following the onset of a weak jet at $t = 0$, superimposed on an isotropic background. The contour plots of the 10-based logarithm of the gas density at t = 30, 60, 90, 133.3, 266.7, and 400 sec. In each panel the axis of symmetry is a horizontal line going through the center. The sunward direction is to the left of each panel. All distances are given in kilometers.

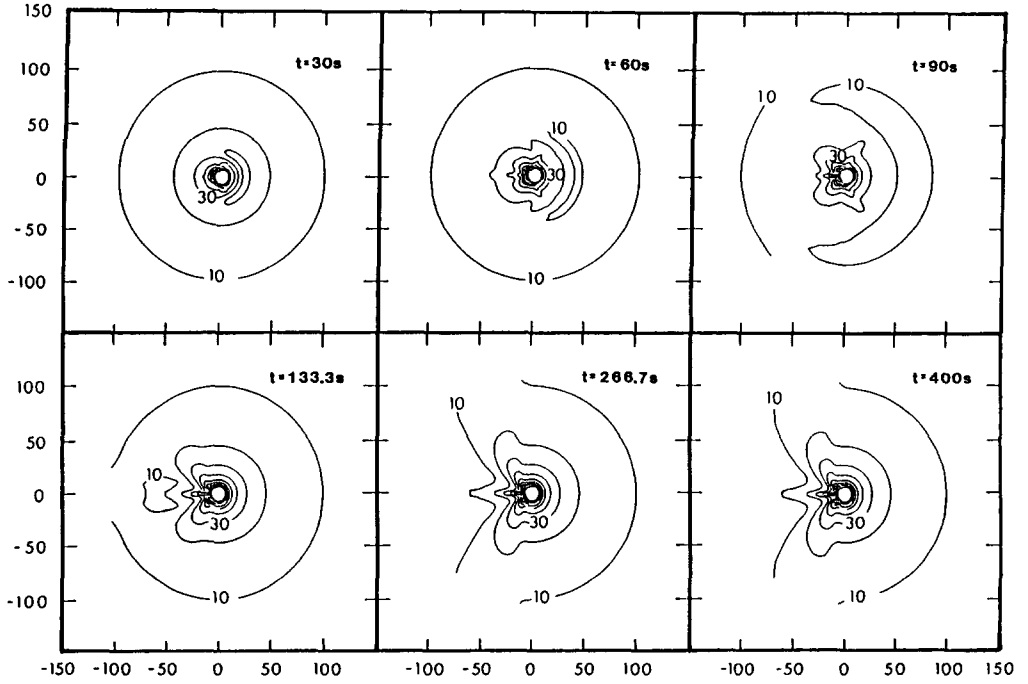

FIG. 3c. Snapshots of constant gas temperature contours following the onset of a weak jet at $t = 0$, superimposed on an isotropic background The panels show the gas temperature contours at $t = 30$, 60, 90, 133.3, 266 7, and 400 sec. In each panel the axis of symmetry is a horizontal line going through the center. The sunward direction is to the left of each panel All distances are given in kilometers

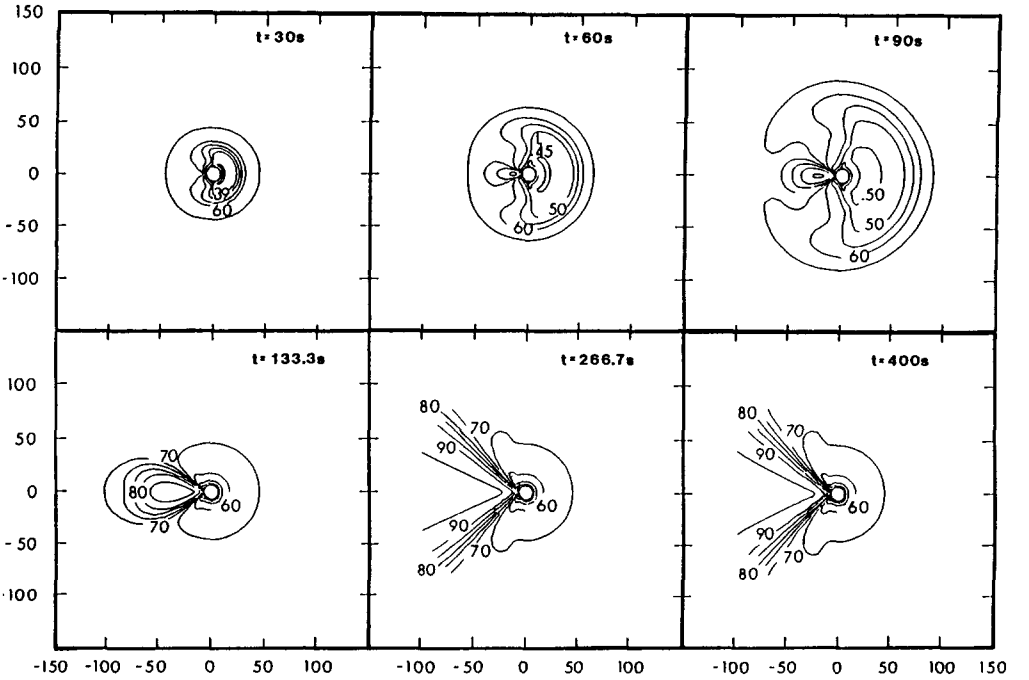

FIG. 3d. Snapshots of constant gas radial velocity contours following the onset of a weak jet at $t = 0$, superimposed on an isotropic background. The panels show the gas radial velocity contours at $t = 30$, 60, 90, 133 3, 266.7, and 400 sec. In each panel the axis of symmetry is a horizontal line going through the center. The sunward direction is to the left of each panel. All distances are given in kilometers

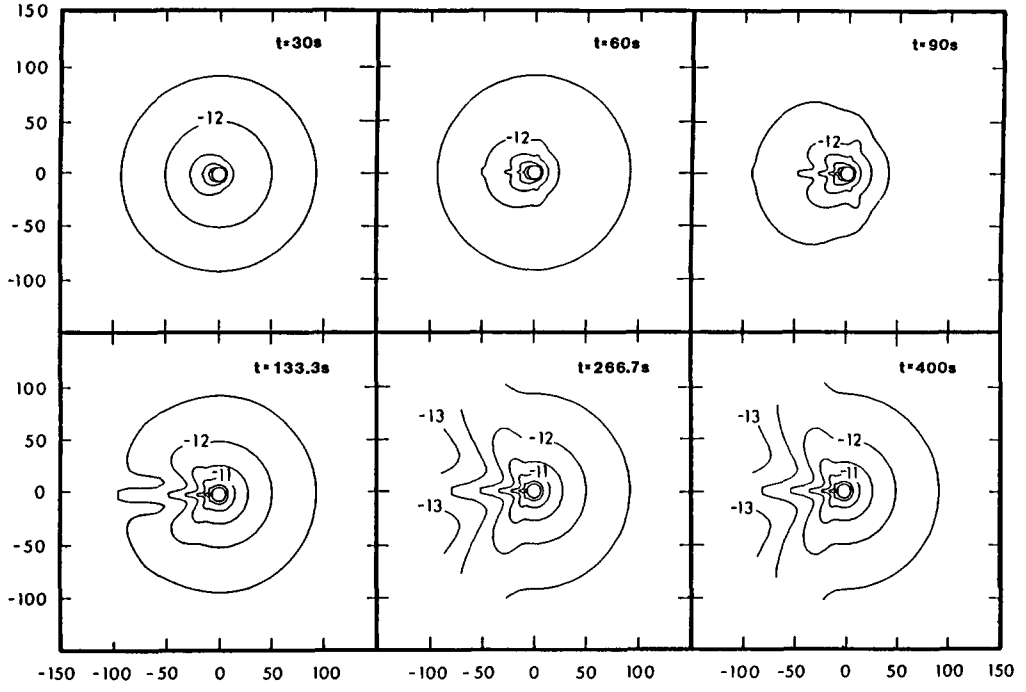

FIG. 3e. Snapshots of constant dust mass density contours following the onset of a weak jet at $t = 0$, superimposed on an isotropic background. The panels show contour plots of the 10-based logarithm of the dust density at t = 30, 60, 90, 133 3, 266.7, and 400 sec. In each panel the axis of symmetry is a horizontal line going through the center. The sunward direction is to the left of each panel. All distances are given in kilometers.

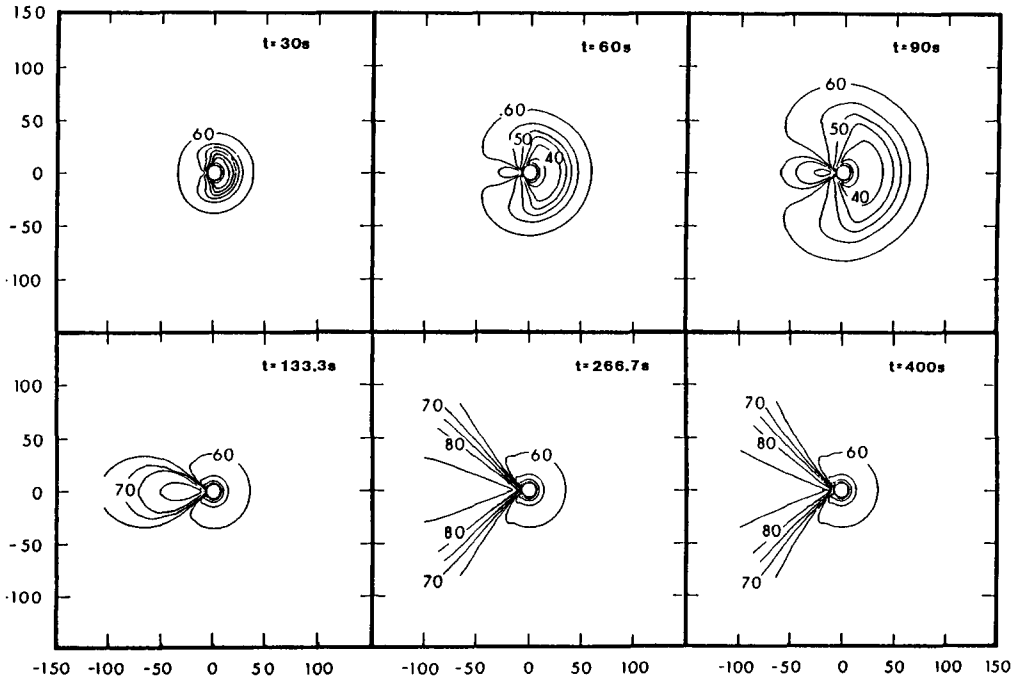

FIG. 3f Snapshots of constant dust radial velocity contours following the onset of a weak jet at $t = 0$, superimposed on an isotropic background. The panels show the dust density contours at t = 30, 60, 90, 133.3, 266.7, and 400 sec. In each panel the axis of symmetry is a horizontal line going through the center. The sunward direction is to the left of each panel All distances are given in kilometers.

The large radial pressure drop generates a radially expanding blast wave, which moves outward with increasing velocity. The radial velocity of the outflowing gas at the nucleus is around 200 m/sec, somewhat smaller than the local speed of sound. This expansion is supported by converting the random energy of the gas molecules into organized translational motion. At the same time the conservation of energy results in a rapid cooling of the expanding gas.

In addition to the large radial pressure gradient, the outflowing gas also has a pressure change in the horizontal direction. However, this horizontal pressure gradient is relatively small compared to the radial one. This modest azimuthal pressure generates a lateral expansion wave propagating in the azimuthal direction with a velocity near the local speed of sound. In the inner region ($r < 3R_N$) the gas temperature is between about 100°K and approximately 150°K; therefore the local sound speed in water vapor is around 250 m/sec. This sound speed is quite comparable to the velocity of radial expansion. In this near nucleus region lateral expansion of the jet ejecta is quite significant: the initial subsolar pressure peak gradually becomes a broadening conical region with a gradually increasing opening angle. For a given cometocentric distance the pressure peak is located on a ring. The axis of symmetry of the ring is pointing along the Sun–comet axis. As the gas moves further from the nucleus the radius of the ring increases and the ring itself broadens. In accordance to the prediction of gas dynamics, the pressure decreases inside the ring. The edges of the ring broaden due to a propagating forward–reverse disturbance pair. Rings originated at different times from the nucleus form a conical region. The development of this cone can be seen in Fig. 3.

Beyond about $3R_N$ the gas temperature decreases to the neighborhood of 10°K; consequently the local sound speed drops to about 75 m/sec, while the radial gas velocity component approaches 1 km/sec. The azimuthal expansion velocity is approximately the same as the local sound speed, which is now about an order of magnitude smaller than the velocity of radial gas expansion; therefore the gas flow becomes nearly radial. In this region the expansion and broadening of the pressure peak ring becomes almost unnoticeable. In the present model all dust particles are of submicron size; therefore the flow pattern of dust particles rapidly accommodates to the changing gas flow. The result is that the azimuthal flow of dust particles also becomes unimportant beyond about $3R_N$. The ring-shaped pressure peak can also be observed in Kitamura's (1986) results, even though he did not discuss its origin in any detail.

Another very interesting new feature of the present solution is the development of subsolar dust spike. Even though this spike is quite noticeable in the present case, it becomes most pronounced in the case of a strong jet with anisotropic background (see Fig. 5). There are two major factors contributing to the formation of this subsolar dust spike. First, the strong horizontal gas flow in the near nucleus region "sweeps" away a large fraction of the dust particles from the region above the edges of the active area (where the horizontal gradient is the largest), thus resulting in a dust density depletion near the edges of the original jet. At the same time the horizontal transport near the axis of symmetry ($\Theta = 0°$) is relatively weak; therefore the jet is only moderately depleted in the central region. The result is a very narrow dust spike just above the center of the active region and a secondary dust accumulation at around $\Theta = 50°$, near the pressure peak cone. Second, the present model considers a comet with about 20 times larger gas production rate and 6 times larger dust production rate than the one described in the K'86 model. Therefore in the present calculation there is about an order of magnitude more dust right above the active spot than in the case considered by the K'86 model. In the im-

mediate vicinity of the nucleus the dust temperature is more than 200°K higher than the gas temperature; therefore the large concentration of hot dust grains just above the surface represents a significant heat source for the outflowing gas and consequently results in significantly elevated gas temperatures (just above the active surface area the gas temperature exceeds the sublimation temperature). The combination of these two processes leads to increased gas and dust velocities along the Sun–comet line (which naturally decreases the dust concentration) as well as to a subsolar dust density peak (due to the horizontal transport generated by the strong lateral pressure gradient at the edges of the jet). These two processes work against each other and the combined result might be either a dust density peak (as it can be seen in the present case) or a dust concentration depletion (as was obtained by Kitamura), depending on the detailed characteristics of the dust production rate profile. The subsolar dust peak cannot be seen in the K'86 model for two reasons: in the K'86 model the absolute dust production was about an order of magnitude smaller and therefore the gas heating by hot grains was much less important than in the present case, and second the K'86 model considered a jet which was about a factor of 2 weaker (with respect to the background) than the present one. The difference between the difference between the results of the K'86 model and our present calculations show that cometary jets might be expected to exhibit widely varying subsolar features depending on the specific nature of the source region itself.

Some narrow features seen in Fig. 3 (and also in subsequent figures) are only a couple of horizontal grid points wide. A natural question is how sure can one be that these features are not computational artifacts? Naturally, a convincing answer would be to increase the grid spacing by at least a factor of 3 and compare the low- and high-resolution results. Our calculations were carried out with the maximum resolution allowed by our computing facilities and resources; therefore such a convincing test could not be carried out. On the other hand the second-order accuracy and the shock capturing nature of the numerical model make it very likely that even narrow features are at least qualitatively real. Based on several test runs when known solutions involving quite narrow features were compared to numerical solutions obtained with our numerical method, we feel fairly confident that the narrow gas and dust features shown in Figs. 3 through 5 are not numerical artifacts.

It is interesting to mention that at $t = 60$ sec and 90 sec a transient feature can be seen in the nightside (at about $= 130°$). This feature can be seen as a small secondary peak in all parameters but the dust velocity. The transient disappears from our integration region by 133.3 sec. The disappearance of this transient clearly coincides with the development of the subsolar dust spike generated by the jet. The physical reason for the transient is that the gas leaves the nucleus with near sonic velocity, while the newly released dust particles have only a negligible initial velocity. This means that in the early phase of the jet the gas blast wave propagates in a practically dust-free space, thus leaving behind the slowly accelerating dust front. There is very little dust loading (momentum and energy transfer from the gas to the dust grains) going on in the almost dust-free region. The lack of significant dust loading results in a smaller momentum (and energy) loss in the expanding gas; therefore there is more random energy available to support the radial and azimuthal gas expansion. This extra random energy translates to higher gas temperature; therefore the jet ejecta can expand into the nightside before adiabatic cooling decreases the local sound speed and consequently the velocity of the azimuthal disturbance to almost negligible values. Between about 60 and 90 sec after onset, the dust acceleration region ($r < 3R_N$) is filled up

with newly ejected dust. The presence of a significant amount of relatively slow dust increases the mass loading of the expanding gas. This increased dust loading results in a pressure decrease in the subsolar acceleration region. Lower gas pressure means that the random energy available to support the lateral expansion is also reduced. The final result of this process is that the laterally expanding gas cools (and consequently slows down) much sooner and therefore the secondary gas and dust peak move back to the dayside from the nightside.

The disappearance of the nighttime pressure peak takes place nearly simultaneously with the development of the subsolar pressure "bite-out." The formation of this low pressure region above the active surface becomes apparent at around $t = 60$ sec. This structure is the direct consequence of the azimuthally propagating gas disturbance: the laterally expanding high pressure ring creates a pressure decrease inside the ring. It can be seen from Figs. 3b and 3c that the same decrease can be observed in the gas density and temperature distributions, meaning that the gas is both transported out of the central region and cooled at the same time.

4.3. Weak Jet with Anisotropic Background

In this calculation a jet strength parameter value of $\alpha = 15$ was adopted, while the gas density in the background reservoir varied as $\rho_{bckg} = \rho_0 \cos \Theta$ for $\cos \Theta > 0.1$ and $\rho_{bckg} = 0.1\ \rho_0$ for $\cos \Theta < 0.1$ ($\rho_0 = 2.5 \times 10^{-9}$ g/cm^3). These parameters resulted in a total gas production rate of 7.9×10^{29} molecules sec^{-1}. The jet/background production rate ratio is 44%; therefore the contribution of the jet to the production rate is about 6.5 times higher than the contribution of Kitamura's (1986) narrow jet.

At $t = 0$ sec the subsolar active area was turned on with an e-folding time of 100 sec and it remained active until the solution reached equilibrium. Well after the new equilibrium was reached, the active region was turned off (at $t = 500$ sec) and the calculation was continued until the original steady-state conditions were reestablished.

Figure 4 shows snapshots of the gas pressure, mass density, temperature, and radial velocity as well as the dust mass density and radial velocity distributions in the inner coma following the onset of a weak dusty jet superimposed on an anisotropic background production. The results are again shown in the same cylindrical coordinate system used in Fig. 3. The individual panels represent snapshots showing projections of two-dimensional equidensity surfaces at $t = 30$, 60, 90, 166.7, 333.3, 500, 600, 700, and 800 sec after the jet was initiated (at $t = 500$ sec the jet was turned off).

Inspection of Fig. 4 reveals that weak jets with isotropic and anisotropic backgrounds show several similarities. The most obvious similarities are the development of the dayside pressure peak cone, the dust accumulation near this cone, the existence of the subsolar dust spike, and pressure bite-out. All these phenomena have been extensively discussed earlier.

On the other hand, there are some notable differences between the flow evolution patterns. The initial steady-state gas and dust flow pattern are not spherically symmetric: there is a gas and dust accumulation cone in the nightside due to the anisotropic background production (the initial solution was obtained as a late time solution with the background gas production only). The initial surface emission peaks at the subsolar point and then slowly decreases as $\cos \Theta$ with increasing zenith angle. For large zenith angles where $\cos \Theta < 0.1$ (this condition is satisfied for $\Theta > 84°$) the surface emission rate is 0.1 times the subsolar production rate. This slowly varying surface production can, in effect, be considered a very broad jet with isotropic background. This physical situation is somewhat similar to our earlier case, when we studied a narrow subsolar jet with isotropic background. The main difference is that in the background case the "jet" is very broad; there-

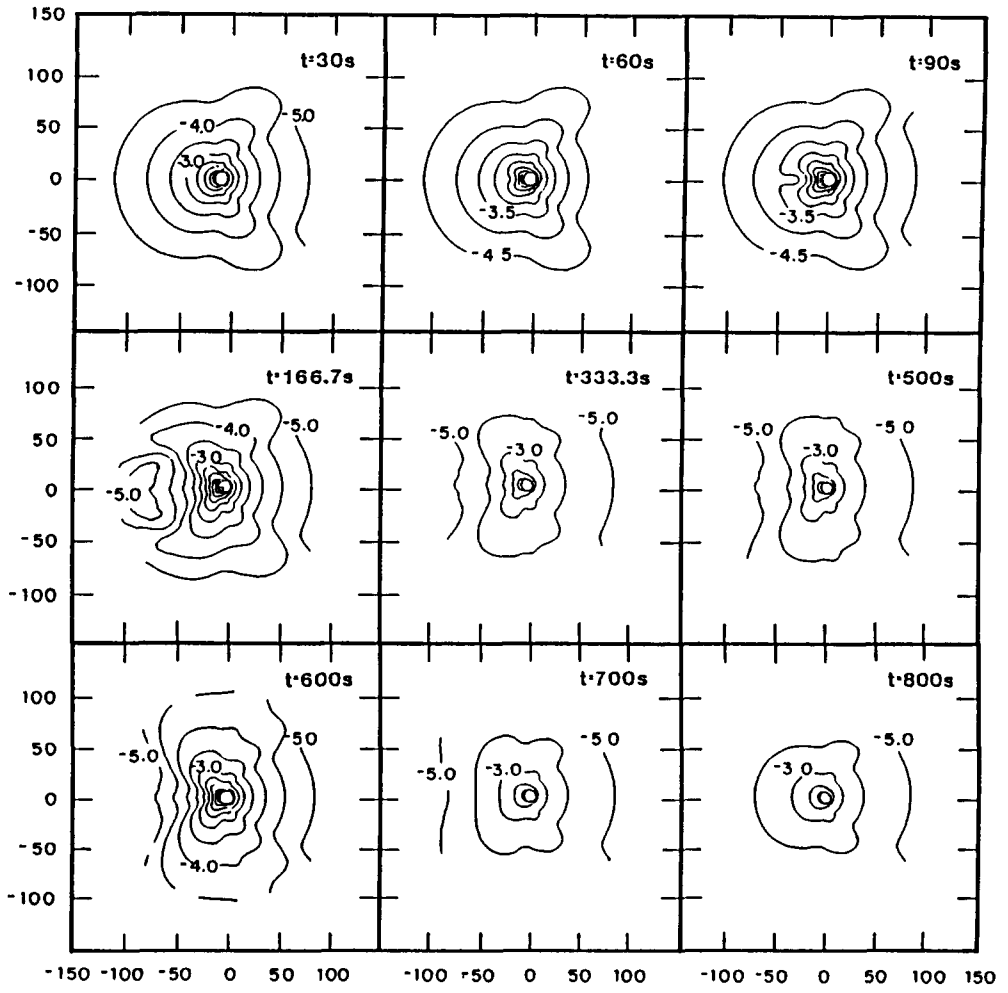

FIG. 4a. Snapshots of constant gas pressure contours following the onset of a weak jet at $t = 0$, superimposed on an anisotropic background. The panels show contour plots of the 10-based logarithm of the gas pressure $t = 30, 60, 90, 166.7, 333.3, 500$ (when the jet was turned off), 600, 700, and 800 sec In each panel the axis of symmetry is a horizontal line going through the center. All distances are given in kilometers.

fore there is only a very small azimuthal pressure gradient even in the immediate vicinity of the nucleus. A natural consequence of this small horizontal pressure gradient is that practically no dust depletion is formed by the practically negligible horizontal gas flow. It should be noted that this initial jet cone expands to the antisunward direction, transporting particles ejected from the dayside beyond the terminator. Another interesting feature of the initial flow pattern is the absence of the subsolar dust spike. This dust spike was not formed in this case because of the very broad nature of the subsolar active region (the effective angular extent of the active area is about 50°).

The general evolution pattern of this jet is quite similar to the one seen in the case of weak jet with isotropic background. At around $t = 60$ sec the subsolar pressure bite-out and the dayside jet cone start to

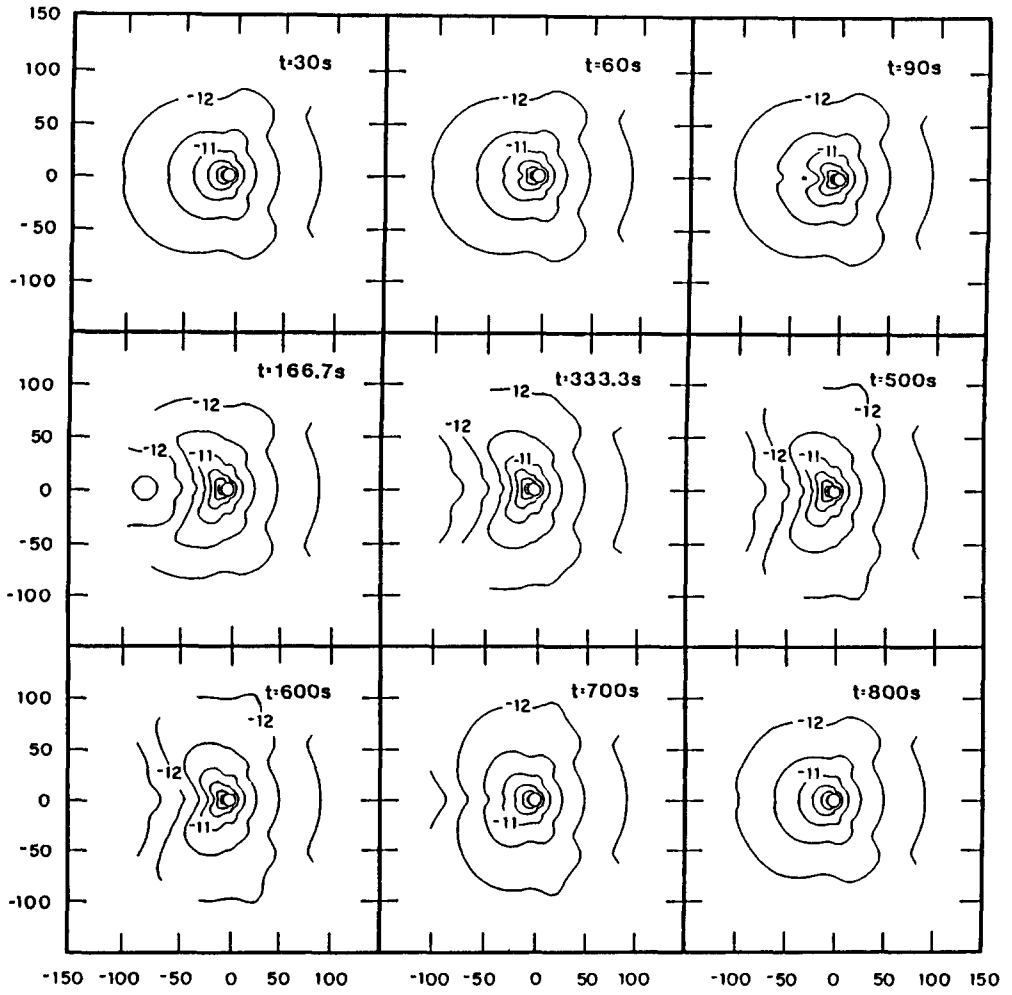

FIG. 4b. Snapshots of constant gas mass density contours following the onset of a weak jet at $t = 0$, superimposed on an anisotropic background. The panels show contour plots of the 10-based logarithm of the gas density at $t = 30$, 60, 90, 166.7, 333 3, 500 (when the jet was turned off), 600, 700, and 800 sec In each panel the axis of symmetry is a horizontal line going through the center The sunward direction is to the left of each panel All distances are given in kilometers

form. This phase of the jet evolution has already been discussed above. An interesting new feature of the present solution is the stable nighttime jet cone, which can be seen in all panels. The reason for the development of two jet cones is quite simple: the model in effect is a superposition of a narrow and a broad jet (the anisotropic background). Both jets create their own jet cone. The jet cone originating from the narrow jet is located in the dayside at around $\Theta \approx 50°$, while the broad jet generated cone extends toward the nightside with an opening angle of about $\Theta \approx 135°$.

The dust density distribution shows a minimum between the two jet cones around $\Theta \approx 110°$. This density minimum becomes apparent at around $t = 166.7$ sec, after the two jet cones have developed. The existence of a minimum between two maxima is of course not surprising at all. However, there is a very interesting feature related to

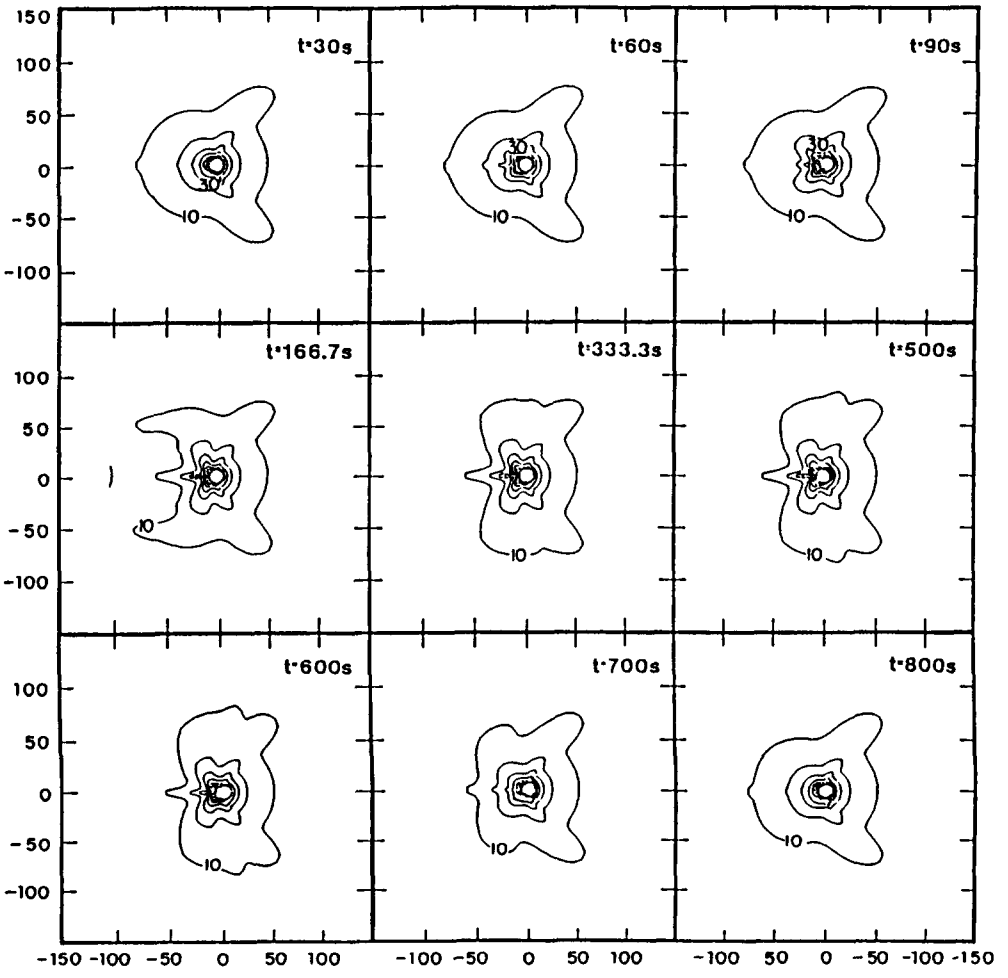

FIG. 4c. Snapshots of constant gas temperature contours following the onset of a weak jet at $t = 0$, superimposed on an anisotropic background The panels show the gas temperature contours at $t = 30$, 60, 90, 166.7, 333 3, 500 (when the jet was turned off), 600, 700, and 800 sec In each panel the axis of symmetry is a horizontal line going through the center. The sunward direction is to the left of each panel. All distances are given in kilometers

this dust density minimum. This interesting feature can be seen in the gas parameters (pressure and density), which at around $\Theta \approx 110°$ show a minimum in the near nucleus region and an additional local maximum at larger cometocentric distances. This phenomenon can be understood in terms of the interplay between horizontal and radial gas and dust transport. The horizontal gas and dust transport is concentrated to the innermost coma, inside about $3R_N$, while beyond this distance the flow is practically radial. This means that in the $r > 3R_N$ region the gas to dust mass ratio does not change significantly and the columns of gas and dust interact like a closed system. The dust to gas mass ratio is larger inside the two jet cones than in the gap between them; therefore inside the gap the radially expanding gas transfers less

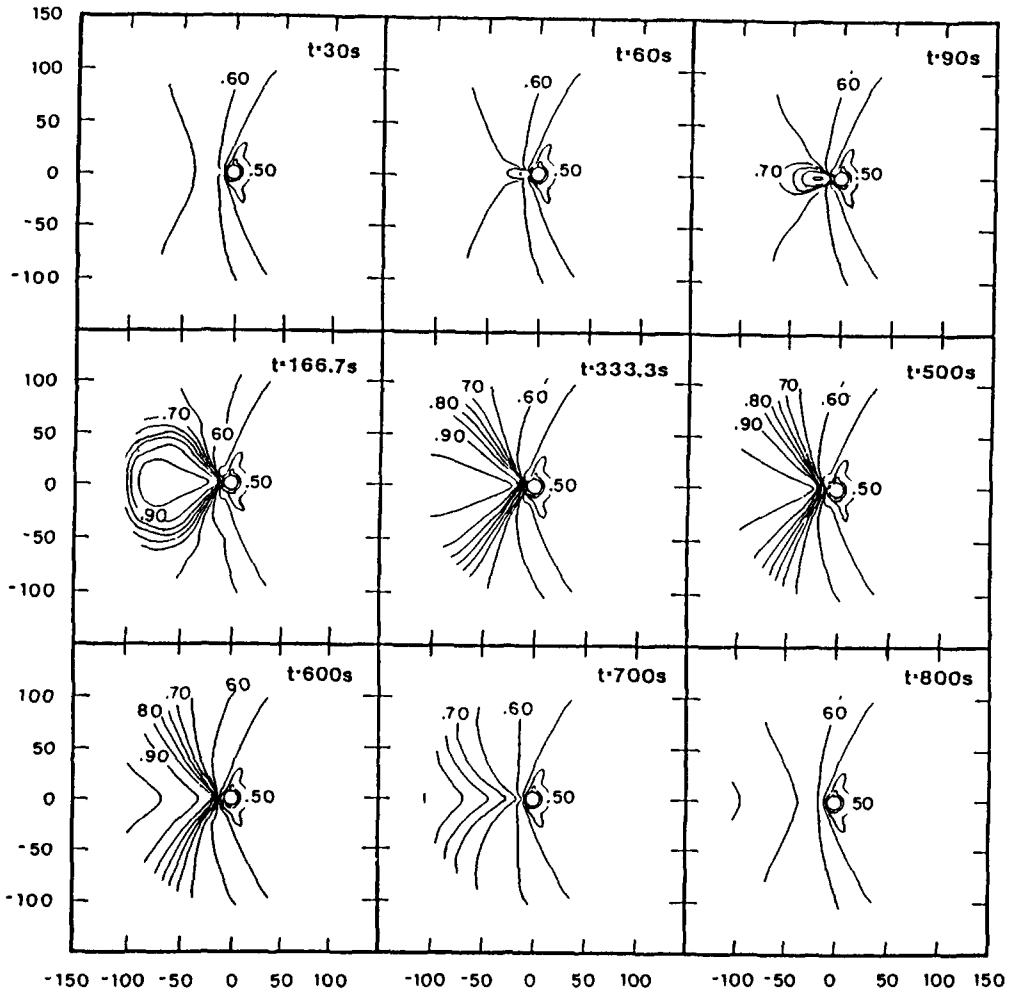

FIG 4d. Snapshots of constant gas radial velocity contours following the onset of a weak jet at $t = 0$, superimposed on an anisotropic background The panels show the gas radial velocity contours at t = 30, 60, 90, 166.7, 333 3, 500 (when the jet was turned off), 600, 700, and 800 sec In each panel the axis of symmetry is a horizontal line going through the center The sunward direction is to the left of each panel All distances are given in kilometers.

momentum and energy to the dust component than inside the jet cones. This results in higher pressure and gas density values beyond ~20 km.

At $t = 500$ sec the jet was turned off with an e-folding time of 100 sec. Following the cutoff of the subsolar narrow active area, the solution returned to the initial gas and dust flow pattern in about 200 sec. The decay of the jet was fairly gradual; no spectacular transient effects were generated during this phase.

4.4. Strong Jet with Anisotropic Background

In this calculation a jet strength parameter value of $\alpha = 75$ was adopted, while the gas density in the background reservoir varied as $\rho_{bckg} = \rho_0 \cos \Theta$ for $\cos \Theta > 0.1$ and $\rho_{bckg} = 0.1\ \rho_0$ for $\cos \Theta < 0.1$ ($\rho_0 = 2.5 \times 10^{-9}$ g/cm^3). These parameters resulted in a total gas production rate of 1.4×10^{30} molecules sec^{-1}. The jet/background production rate ratio is 1.88 (jet/total ratio

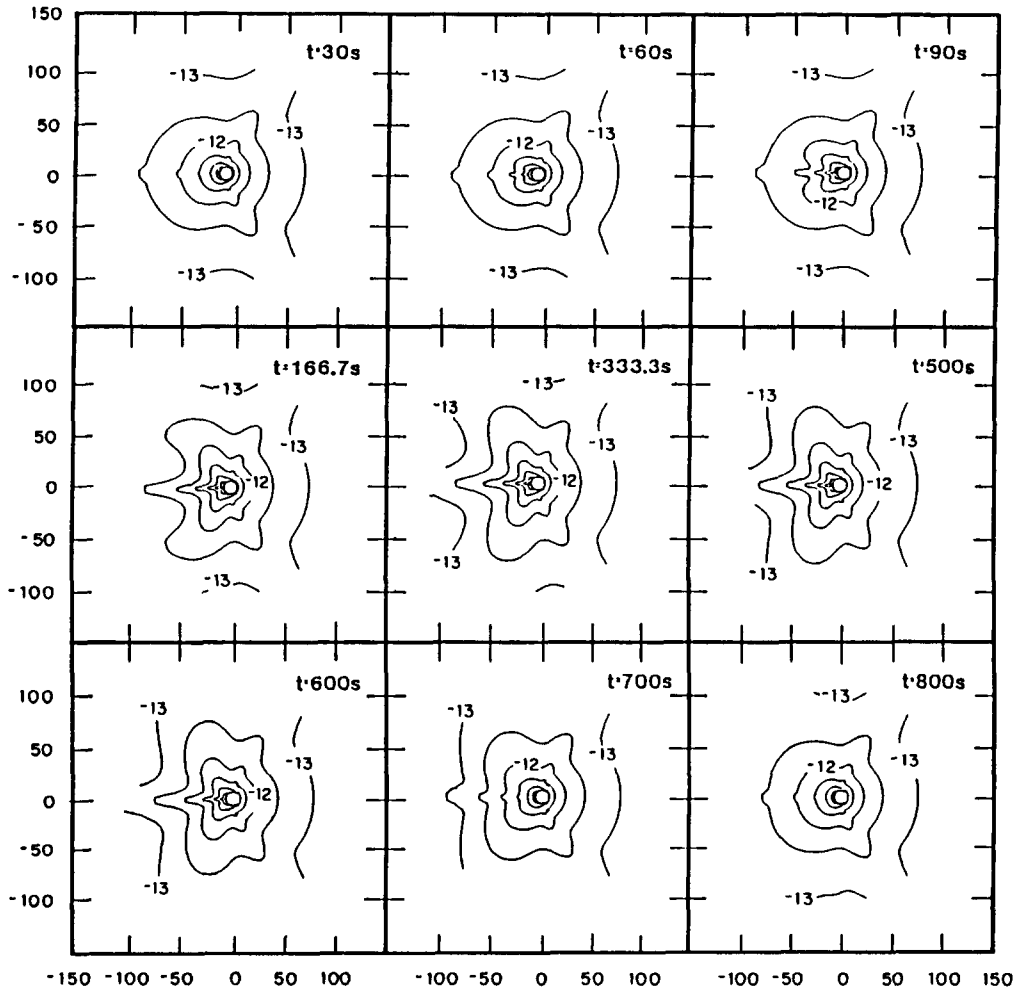

FIG. 4e Snapshots of constant dust mass density contours following the onset of a weak jet at $t = 0$, superimposed on an anisotropic background. The panels show contour plots of the 10-based logarithm of the dust density at t = 30, 60, 90, 166.7, 333 3, 500 (when the jet was turned off), 600, 700, and 800 sec In each panel the axis of symmetry is a horizontal line going through the center The sunward direction is to the left of each panel. All distances are given in kilometers.

is 0.65); therefore, the contribution of the jet to the total production rate is about 10 times higher than the contribution of Kitamura's (1986) narrow jet (the jet/total production rate ratio in the K'86 model was 0.07). At $t = 0$ sec the subsolar active area was turned on with an e-folding time of 100 sec and it remained active until the solution reached equilibrium.

Figure 5 shows snapshots of the gas pressure, mass density, temperature, and radial velocity as well as the dust mass density and radial velocity distributions in the inner coma following the onset of a strong dusty jet superimposed on an anisotropic background production. The results are again shown in the same cylindrical coordinate system used in Fig. 3. The individual panels represent snapshots showing projections of two-dimensional equidensity surfaces at t = 30, 60, 90, 133.3, 266.7, and 400 sec after the jet was initiated.

The initial condition is the same as it was

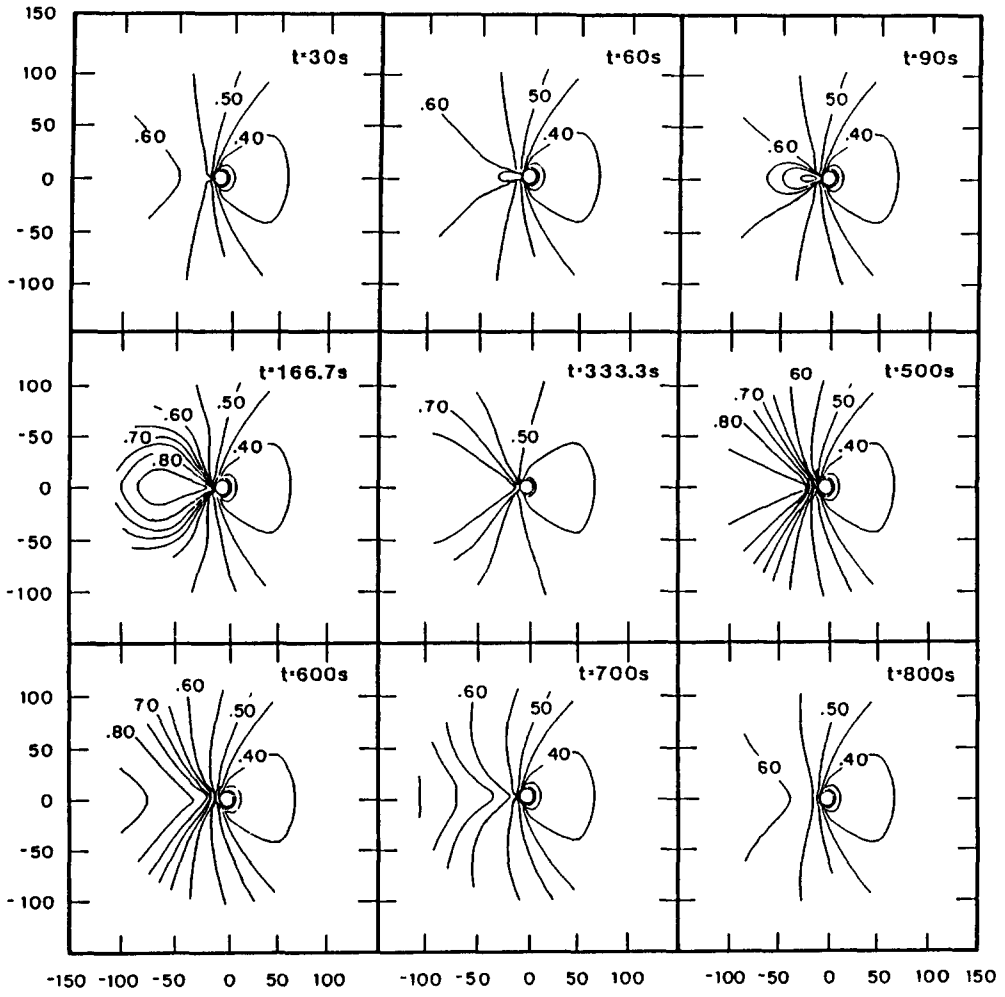

FIG. 4f. Snapshots of constant dust radial velocity contours following the onset of a weak jet at t = 0, superimposed on an isotropic background. The panels show the dust radial velocity contours at t = 30, 60, 90, 166.7, 333.3, 500 (when the jet was turned off), 600, 700, and 800 sec In each panel the axis of symmetry is a horizontal line going through the center The sunward direction is to the left of each panel. All distances are given in kilometers

in the previous case, when we calculated the evolution of a weak subsolar jet with anisotropic background. At around t = 60 sec the subsolar pressure bit-out and related phenomena start to develop, in a manner very similar to that in our earlier calculations. A very interesting aspect of the results is that in the present calculation the primary dust cone is pushed back to the nightside, with a half-opening angle of about 150°. This result basically means that beyond about 50 km or so the dust density peak is located at the nightside. As will be discussed, this result seems to be in a good agreement with the Giotto observations.

An interesting feature of the solution is the development of a very pronounced gas temperature spike near the Sun–comet line. Inspection of Fig. 5 reveals that this temperature spike is accompanied by a deple-

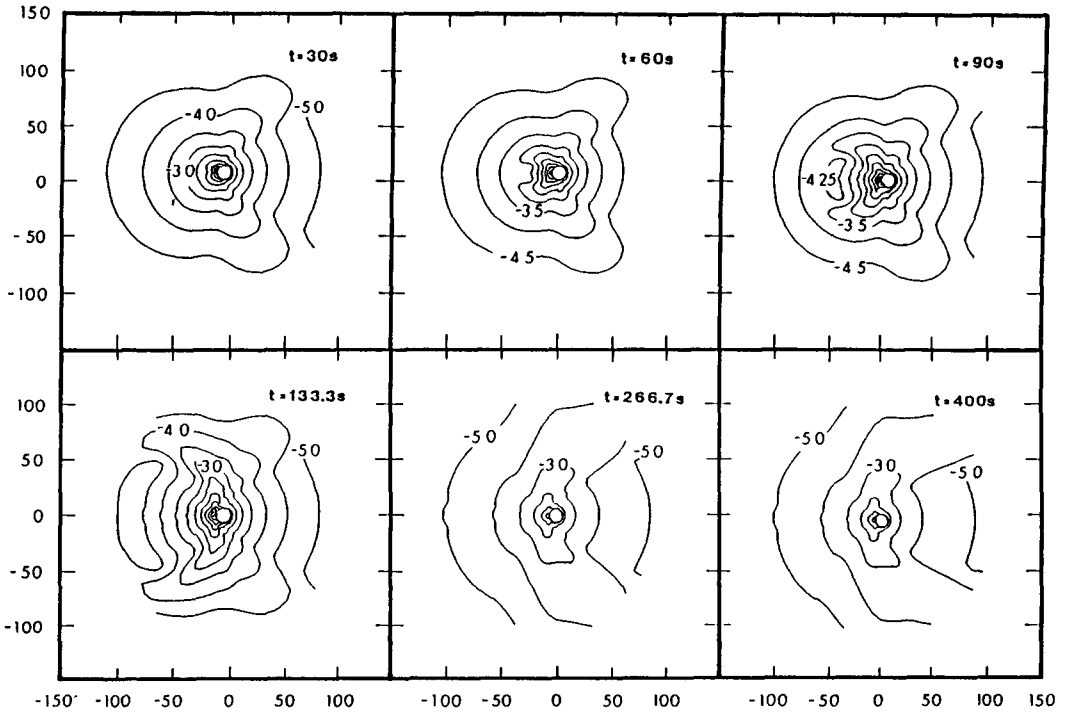

FIG. 5a. Snapshots of constant gas pressure contours following the onset of a strong jet at $t = 0$, superimposed on an anisotropic background The panels show contour plots of the 10-based logarithm of the gas pressure at $t = 30$, 60, 90, 133.3, 266.7, and 400 sec. In each panel the axis of symmetry is a horizontal line going through the center. All distances are given in kilometers.

tion of gas density and by a dust density spike. The gas pressure is slightly elevated in this region, but this parameter does not show a spikelike structure. If anything, there seems to be an approximate pressure balance throughout the subsolar spike region. This phenomenon can be explained by the dust heating process (the dust temperature is much higher than the gas temperature; therefore the large concentration of hot grains just above the active surface area represents a significant heat source for the thermally accommodated reflected gas molecules) and by the lack of significant azimuthal transport in the immediate vicinity of the Sun–comet line. In this region the horizontal transport is negligible; therefore the gas expansion is nearly spherically symmetric. This means that in the subsolar region the adiabatic cooling of the gas is much slower than at higher zenith angles, where azimuthal expansion also decreases the gas temperature. The decreased gas density in the subsolar region is a direct consequence of the temperature spike: the elevated gas temperature is able to generate higher radial expansion velocities, which result in lower gas densities.

Another feature of the strong jet is the very large opening angle of the jet cone. This is particularly interesting because the gas temperature in the sublimation reservoir is the same as it was in the previous two cases and the temperature structure in the innermost coma is somewhat similar to the weak jet case. Earlier we argued that in the case of the jet the lateral expansion was basically a disturbance propagating with the local speed of sound. This argument is not true in the present physical scenario. In the

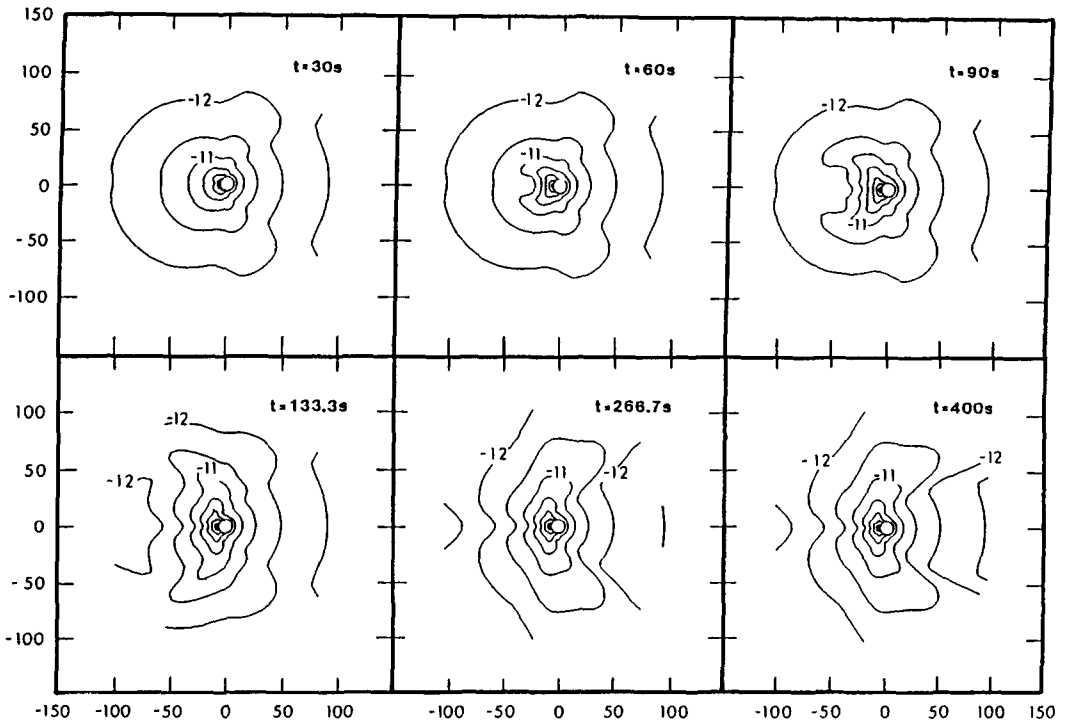

FIG. 5b. Snapshots of constant gas mass density contours following the onset of a strong jet at $t = 0$, superimposed on an anisotropic background. The panels show contour plots of the 10-based logarithm of the gas density at $t = 30$, 60, 90, 133 3, 266.7, and 400 sec. In each panel the axis of symmetry is a horizontal line going through the center. The sunward direction is to the left of each panel All distances are given in kilometers.

case of a strong jet the lateral pressure gradient near the edge of the narrow, subsolar jet is large enough to generate a strong shock wave. Initially this shock wave propagates with a highly supersonic velocity in the ambient gas. Later the laterally propagating shock significantly weakens and it continues its azimuthal expansion as a disturbance propagating with slightly supersonic velocities.

5. DISCUSSION

The first results obtained with our time-dependent, axisymmetric dusty gas dynamic model, which solves the coupled partial differential equation system describing the flow of dust and gas in the inner cometary coma, show a flow structure more or less similar to the results published by Kitamura (1986). The difference between the two sets of calculations is due mainly to the different inner boundary conditions. Both calculations predict the development of jet cones, which are regions of gas and dust accumulation bounded by conical surfaces, and are formed around $2\text{–}3R_N$. At the jet cones the azimuthal expansion velocities become negligible with respect to the radial component of the flow velocity. Therefore this region is characterized by an accumulation of gas and dust. Jet cones are formed by an interplay between the strong adiabatic cooling of the rapidly expanding gas and the relatively modest horizontal pressure gradient. The weak azimuthal pressure gradient generates a disturbance wave in the gas which expands in the horizontal direction with a propagation velocity slightly

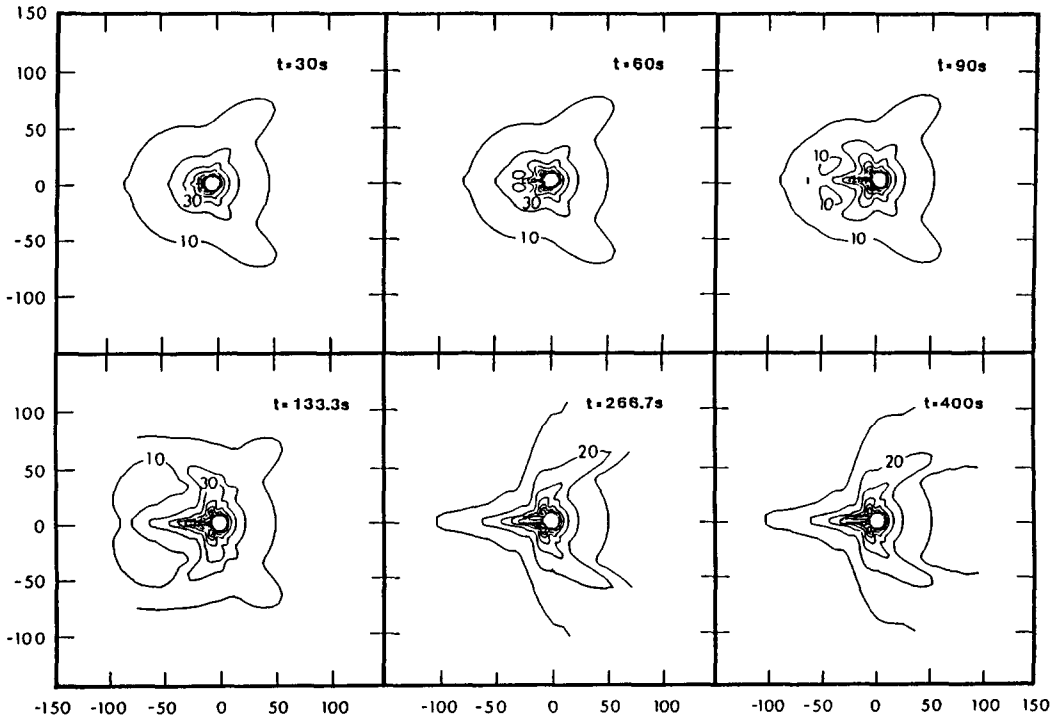

FIG. 5c Snapshots of constant temperature contours following the onset of a strong jet at $t = 0$, superimposed on an anisotropic background. The panels show the gas temperature contours at $t = 30$, 60, 90, 133 3, 266 7, and 400 sec. In each panel the axis of symmetry is a horizontal line going through the center. The sunward direction is to the left of each panel All distances are given in kilometers.

exceeding the local speed of sound. At cometocentric distances of about $3R_N$ the local sound speed is around 75 m/sec, which is about an order of magnitude smaller than the radial gas velocity. At around this distance the dusty gas flow becomes approximately radial and the jet cone is formed.

The present set of calculations revealed that the half-opening angle of jet cones is about 50° for narrow, weak jets. This value remains more or less constant as long as the horizontal pressure gradient at the surface does not exceed a critical value. Above this critical pressure gradient the azimuthal pressure gradient generates a strong shock propagating in the horizontal direction well above the local speed of sound. In the case of strong jets the horizontal pressure gradient is larger than the critical value; therefore the initial lateral expansion of the jet ejecta is supersonic, resulting in a jet cone half-opening angle exceeding 90°. The strong jet produces an "apparent" nighttime source of gas and dust production. At the same time it should be mentioned that anisotropic background production (very broad jet) is also producing a weaker, but noticeable nighttime jet cone. Therefore the formation of the nighttime dust accumulation is not a unique consequence of strong, narrow jets.

The Comet Halley images taken by the Giotto spacecraft revealed a nighttime dust component >30 km from the nucleus (Keller *et al.* 1987, and H. U. Keller, private communication 1988). This dust population was interpreted by the Giotto imaging team as dust grains originating from the active areas on the dayside and swept across the

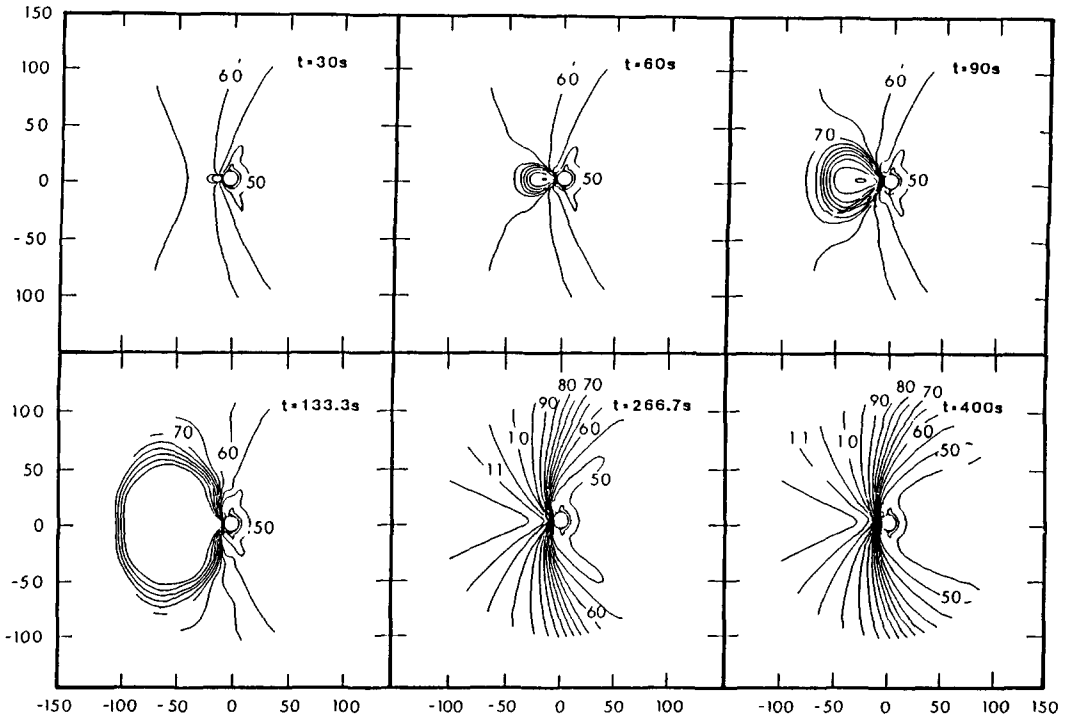

FIG 5d Snapshots of constant gas radial velocity contours following the onset of a strong jet at t = 0, superimposed on an anisotropic background. The panels show the gas radial velocity contours at t = 30, 60, 90, 133 3, 266 7, and 400 sec. In each panel the axis of symmetry is a horizontal line going through the center. The sunward direction is to the left of each panel All distances are given in kilometers

terminator by the expanding gas (H. U. Keller, private communication 1988). The present set of calculations supports this idea and offers detailed quantitative predictions to be compared with the Giotto images.

The present calculations show a narrow subsolar dust density spike along the Sun–comet line. This spike cannot be seen in Kitamura's (1986) results. This spike is formed as a consequence of two physical processes. First, in the immediate vicinity of the nucleus the dust temperature is still very close to the surface temperature, and the large concentration of hot dust grains just above the active region represents a significant heat source for the thermally accommodated reflected gas molecules. The second reason is that the gas has no azimuthal velocity component along the axis of symmetry (the Sun–comet line); therefore the dust cannot be swept away from this region. It is interesting to note that Kitamura's (1986) results show a broad subsolar dust density peak with a bite-out along the Sun–comet axis. This density bite-out is a consequence of higher radial dust velocities along this line. It can be seen from Figs. 18, 19, and 20 of Kitamura's (1986) paper that his radial dust velocity peaks at $\Theta = 0°$, while the horizontal dust velocity is practically zero near the Sun–comet line. The horizontal variation of the dust density is quite slow near the axis of symmetry and the conservation of dust flux therefore results in a small subsolar dust density minimum. On the other hand, in our weak jet model the dust density increase with re-

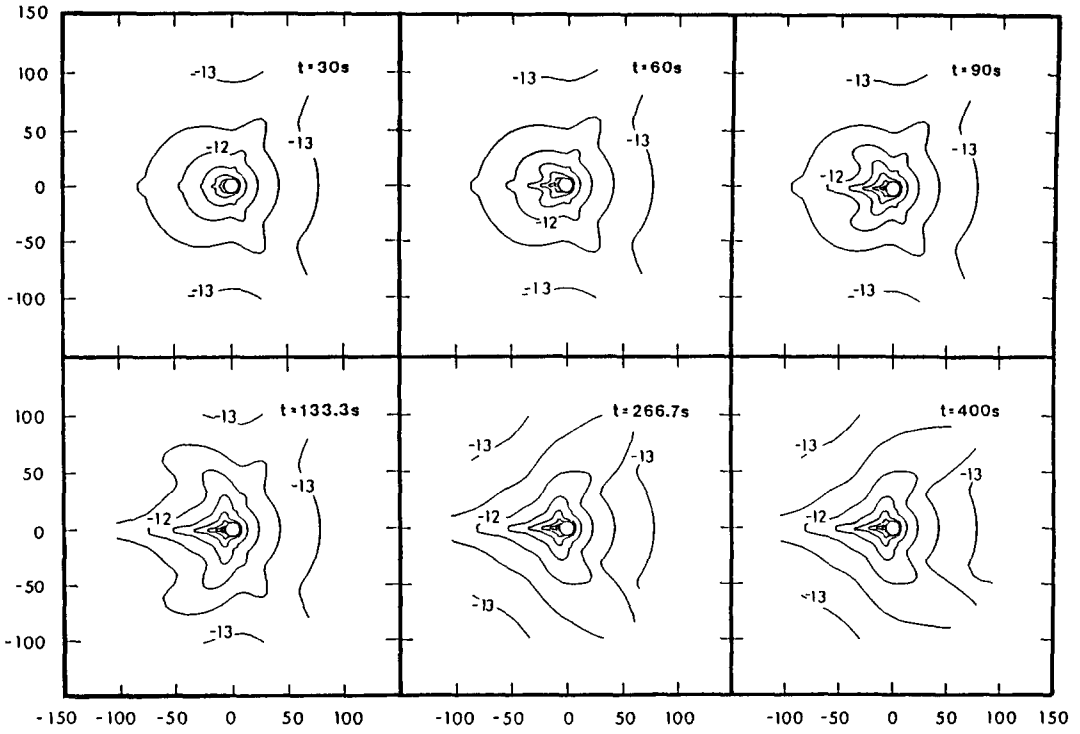

FIG. 5e. Snapshots of constant dust mass density contours following the onset of a strong jet at $t = 0$, superimposed on an anisotropic background The panels show contour plots of the 10-based logarithm of the dust density at $t = 30$, 60, 90, 133 3, 266 7, and 400 sec. In each panel the axis of symmetry is a horizontal line going through the center The sunward direction is to the left of each panel. All distances are given in kilometers

spect to the isotropic background is about a factor of 2, while the absolute amount of dust is about six times larger than that in Kitamura's (1986) calculation. In our case the stronger jet results in more gas heating and in a larger density gradient near the axis of symmetry; therefore the dust density decrease due to the increased radial dust flow velocity is unable to offset the azimuthal decrease of the surface dust density. This difference in the results shows how strong an influence the detailed initial conditions have on the structure of the dust distribution near the center of the jet. At the same time some other features (such as the formation of the jet cone) seem to be much less sensitive to the strength and structure of the source region.

Our results have some potentially important consequences for future comet missions and for interpreting remote near-Earth observations of cometary dust features observed from Earth orbit. First, the "safest" location for making close-up observations of an active cometary region seems to be at a cometocentric distance of several comet radii and about 25° away from the jet axis: this is the region where the dust density shows a local minimum for both weak and strong jets. The regions with the highest dust density values are near the jet axis and in the vicinity of the jet cone. The half-opening angle of the jet cone is a function of the jet strength and therefore its location is very difficult to predict. Another consequence of our results is that during the initial, transient phase of the outburst the opening angle of jet cone varies considerable. Shortly after the onset of the active region the half-opening angle is larger than

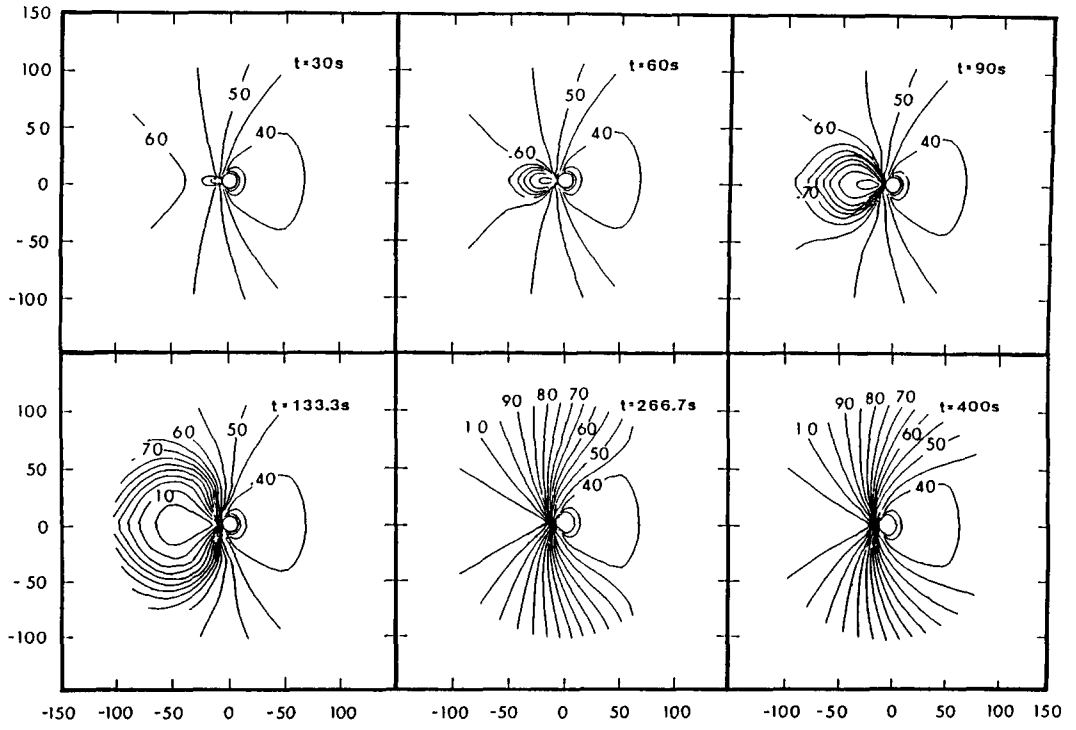

FIG. 5f Snapshots of constant dust radial velocity contours following the onset of a strong jet at t = 0, superimposed on an isotropic background The panels show the dust radial velocity contours at t = 30, 60, 90, 133 3, 266.7, and 400 sec. In each panel the axis of symmetry is a horizontal line going through the center The sunward direction is to the left of each panel. All distances are given in kilometers

~100° even in the case of weak jets. By about 5 min after the beginning of the outburst the equilibrium dust cone is formed at much smaller zenith angles. This means that the first few minutes of an outburst represents an increased dust hazard in a fairly broad region extending from about 50 to about 130°.

The results of the present calculations should also make us quite cautious when interpreting the observed morphological features of cometary dust comae. It is obvious that the source regions of the observed dust features do not necessarily coincide with the "foot" of these structures obtained by extrapolating the observed curvatures toward the nucleus. The dust and gas transport in the nucleus–coma interface region ($>3R_N$) is highly nonradial; therefore it is very difficult to determine the real source regions of cometary activity from remote observations of dust morphology.

6. SUMMARY

This paper presents the first results of a new time-dependent, axisymmetric dusty gas dynamic model of inner cometary atmospheres. The model solves the coupled, time-dependent continuity, momentum, and energy equations for a gas–dust mixture between the nucleus surface and 100 km using a 40 × 40 axisymmetric grid structure. The time-dependent multidimensional partial differential equation system was solved with a new numerical technique employing a second-order accurate Godunov-type scheme with dimensional splitting.

Three sets of calculations have been car-

ried out with the model. The first of these calculations describes the evolution of a weak subsolar jet superimposed on an isotropic background. The second calculation considers the same active area in the presence of an anisotropic background source, while the third calculation describes the evolution of a strong jet with anisotropic background.

The results of the first run were compared to the results of a similar model of Kitamura (1986). The general features of our run describing a weak jet with isotropic background and those of Kitamura (1986) are quite similar with the exception of the subsolar dust spike, the formation of which strongly depends on the strength and structure of the source region. The present model predicts a narrow, subsolar dust density spike, which cannot be seen in Kitamura's (1986) results.

Our main conclusions are the following:

1. Narrow axisymmetric jets (characteristic angular is 10°) generate a subsolar dust spike and a jet cone, where a significant amount of the jet ejecta is accumulated. This subsolar jet spike has not been predicted by earlier calculations. The opening angle of the jet cone varies during the time-dependent phase of the jet. For weak jets the steady-state half opening angle is about 50°. In the case of the strong jets the jet cones extend to the nightside and they might have an "apparent" source region in the nightside, in good agreement with Giotto imaging results.

2. Subsolar jet spikes are formed as a consequence of two physical processes. First, the dust temperature is much higher than the gas temperature; therefore the large concentration of slow, hot dust grains just above the active region represents a significant heat source for the thermally accommodated reflected gas molecules. The second reason is that the gas has no azimuthal velocity component along the axis of symmetry (the Sun–comet line); therefore the dust cannot be swept away from this region.

3. The physical reason for the formation of the jet cones is the difference between the horizontal and the radial gas pressure gradients. The gas always expands radially into a low-pressure external medium. The horizontal pressure difference is much smaller and is able to generate only a relatively weak disturbance propagating somewhat above the local speed of sound. The temperature decreases to the vicinity of 10° by about $3R_N$ (primarily due to adiabatic cooling). Therefore beyond this cometocentric distance the radial flow velocity becomes about an order of magnitude larger than the azimuthal velocity of the jet ejecta. The result is an accumulation of nearly radially propagating gas and dust; this accumulation was termed jet cone.

4. In the early phase of the jet development an interesting transient gas and dust peak can be seen in the nightside (at about $\Theta = 130°$). The disappearance of this transient coincides with the development of the subsolar dust spike. The explanation is that in the early phase of the jet evolution the gas blast wave propagates in a practically dust-free space, thus leaving behind the slowly accelerating dust front. The lack of significant dust loading in this phase results in a smaller momentum (and energy) loss of the expanding gas. Therefore there is more random energy available to support the radial and azimuthal gas expansion and the jet ejecta can expand into the nightside before adiabatic cooling decreases the local sound speed (and consequently the velocity of the azimuthal disturbance) to small values with respect to the radial flow velocity. In the latter stage of the jet evolution the main dust acceleration region ($r < 3R_N$) is filled up with newly ejected dust. The presence of a significant amount of relatively slow dust increases the mass loading of the expanding gas and results in a pressure decrease in the subsolar acceleration region. The final result of this process is that the cooling of the laterally expanding gas becomes more efficient and therefore the gas

and dust peak (the jet cone) moves back to the dayside from the nightside.

5. In the case of anisotropic backgrounds two jet cones were obtained. The first jet cone is related to the jet itself, while the second cone with a half-opening angle of about 135° is generated by the background pressure gradient: the background itself can be considered to be a very broad jet. However, the anisotropic background does not contribute to the formation of the subsolar dust spike.

APPENDIX. THE NUMERICAL METHOD

The coupled, time-dependent continuity, momentum, and energy equations for a dust–gas mixture (Eq. (2) through (12)) were solved using a second-order accurate Godunov-type scheme with dimensional splitting. This new numerical scheme has recently been developed by the authors with the advice of Dr. Bram van Leer. This technique is applicable to initial value problems governed by hyperbolic partial differential equations. Because the present model is the first full-scale application of this new numerical technique, we feel that it is appropriate to describe the main features of this technique.

Let us consider the following general form of the Euler equations describing the conservation equations for a two-dimensional, inviscid compressible gas with external sources and sinks,

$$\frac{\partial \mathbf{w}}{\partial t} + \frac{1}{r^2}\frac{\partial (r^2 \mathbf{G})}{\partial r} + \frac{1}{r \sin \Theta}\frac{\partial (\sin \Theta\, \mathbf{H})}{\partial \Theta} = \mathbf{S}, \tag{A1}$$

where t is time, r is radius, Θ is azimuth angle and

$$\mathbf{w} = \begin{bmatrix} \rho \\ \rho u_r \\ \rho u_\Theta \\ \rho e \end{bmatrix}, \quad \mathbf{G} = \begin{bmatrix} \rho u_r \\ \rho u_r^2 + p \\ \rho u_r u_\Theta \\ u_r(\rho e + p) \end{bmatrix},$$

$$\mathbf{H} = \begin{bmatrix} \rho u_\Theta \\ \rho u_r u_\Theta \\ \rho u_\Theta^2 + p \\ u_\Theta(\rho e + p) \end{bmatrix}, \quad \mathbf{S} = \begin{bmatrix} 0 \\ \frac{2}{r} p - F_{\mathrm{gd},r} \\ -F_{\mathrm{gd},\Theta} \\ Q_{\mathrm{ext}} - Q_{\mathrm{gd}} \end{bmatrix}. \tag{A2}$$

Here ρ is gas density, p is pressure, and e is specific total energy, while u_r and u_Θ are the radial and azimuthal velocity components, respectively.

Equation (A1) describing the axisymmetric flow of the gas component was solved using a second-order accurate Godunov-type scheme with dimensional splitting (the dust equations were solved with a simpler method). This technique is applicable to initial value problems governed by hyperbolic partial differential equations. It can be shown (Gourlay and Morris 1970) that the second-order accurate two-dimensional operator, $L_{r,\Theta}(\Delta t)$, which integrates the system of conservation equations from time t to $t + \Delta t$, can be "split" into the following sequence of one-dimensional operators,

$$L_{r,\Theta}(2\Delta t) = L_r(\Delta t) L_\Theta(\Delta t) L_\Theta(\Delta t) L_r(\Delta t), \tag{A3}$$

where L_Θ and L_r represent second-order accurate one-dimensional time step operators obtained by omitting the **G** and **H** flux vectors, respectively. This way the problem reduces to the determination of a second-order accurate method with one spatial dimension.

Let the second-order accurate one-dimensional operator, L, denote a time step in the radial or azimuthal direction, which integrates the following system of conservation equations from time t to $t + \Delta t$,

$$\frac{\partial \mathbf{w}}{\partial t} + \frac{\partial \mathbf{F}}{\partial x} = \mathbf{P}, \tag{A4}$$

where

$$\frac{\partial \mathbf{F}}{\partial x} = \frac{1}{r^2}\frac{\partial (r^2 \mathbf{G})}{\partial r} \quad \text{or}$$

$$\frac{\partial \mathbf{F}}{\partial x} = \frac{1}{r \sin \Theta}\frac{\partial (\sin \Theta\, \mathbf{H})}{\partial \Theta} \tag{A5}$$

and $\mathbf{P(G)} + \mathbf{P(H)} = \mathbf{S}$.

The spatial region to be modeled is divided into cells. A set of flow parameters is attributed to the center of each cell. The time evolution of the cell parameters is calculated by a predictor–corrector version of a second-order upwind scheme, based on Fromm's (1968) convection scheme (B. van Leer, private communication 1987),

$$w_j^{n+1} = w_j^n - \frac{\Delta t}{\Delta x_j}(\mathbf{F}_{j+1/2}^{n+1/2} - \mathbf{F}_{j-1/2}^{n+1/2}) + \Delta t\, \mathbf{P}_j^{n+1/2}, \tag{A6}$$

where the upper index denotes time and the lower one is the serial number of spatial cells. The index of $j + 1/2$ refers to the boundary cells j and $j + 1$, while time $n + 1/2$ corresponds to the middle of the time interval. In order to calculate the fluxes of conserved quantities at the cell boundaries, one must adopt an interpolating expression to describe the variation of gas parameters within one spatial cell. Linear interpolation within each cell will ensure second-order accuracy of the overall method: to eliminate numerical oscillations near discontinuities in the solution, the interpolation method must be "monotonicity preserving" or "nonoscillatory" (van Leer 1977). In the present algorithm the following nonlinear, upwind-biased interpolation was adopted (van Leer, private communication 1988),

$$\mathbf{w}_{j+1/2,L}^n = \mathbf{w}_j^n + \frac{1}{2}\Delta x_j R\left(\frac{\Delta_+ \mathbf{w}_j^n}{\Delta_- \mathbf{w}_j^n}\right)\frac{\Delta_+ \mathbf{w}_j^n + \Delta_- \mathbf{w}_j^n}{2} \tag{A7}$$

$$\mathbf{w}_{j-1/2,R}^n = \mathbf{w}_j^n - \frac{1}{2}\Delta x_j R\left(\frac{\Delta_+ \mathbf{w}_j^n}{\Delta_- \mathbf{w}_j^n}\right)\frac{\Delta_+ \mathbf{w}_j^n + \Delta_- \mathbf{w}_j^n}{2}, \tag{A8}$$

where

$$\Delta_+ \mathbf{w}_j^n = 2\frac{\mathbf{w}_{j+1}^n - \mathbf{w}_j^n}{\Delta x_{j+1} + \Delta x_j} \tag{A9}$$

$$\Delta_- \mathbf{w}_j^n = 2\frac{\mathbf{w}_j^n - \mathbf{w}_{j-1}^n}{\Delta x_j + \Delta x_{j-1}} \tag{A10}$$

$$R(\vartheta) = \frac{2\vartheta}{1 + \vartheta^2}. \tag{A11}$$

This version of the monotonicity function, R, enhances the sharpness of the shock structure at cell boundaries and results in upwind-biased derivatives. The interpolation technique results in second-order accuracy and it also eliminates some discontinuities with nonphysical entropy change, which are not filtered out by Roe's (1981) Riemann solver (Harten *et al.*, 1983) adopted in the present model.

In the next step we calculate the flux values across the cell boundaries. In order to obtain these values a Riemann problem is solved at each cell boundary (a Riemann problem is a set of conservation equations with a discontinuous initial condition). In our case the solutions of these Riemann problems describe three waves at each cell boundary: the inner one is a contact discontinuity, while the other ones are either shock waves or rarefaction waves. The present scheme utilizes a slightly modified version of Roe's (1981, 1986) Riemann solver. These modifications (B. van Leer, private communication 1987) were necessary to enable us to take into account the source terms and the interpolating formulas (A7) and (A8).

Consider a one-dimensional Riemann problem for a set of linear conservation laws with the following initial condition:

$$\mathbf{w}(x, 0) = \begin{cases} \mathbf{w}_L + x\mathbf{d}_L & x < 0 \\ \mathbf{w}_R + x\mathbf{d}_R & x > 0. \end{cases} \tag{A12}$$

In the case of linear conservation laws the conservation equations can also be expressed in the form

$$\frac{\partial \mathbf{w}}{\partial t} + A\frac{\partial \mathbf{w}}{\partial x} = \mathbf{P}, \tag{A13}$$

where A is a constant Jacobian matrix, $A = \partial \mathbf{F}/\partial \mathbf{w}$. Let U denote a matrix, with columns composed of the right eigenvectors of A. It is obvious that A can be expressed as

$$A = U \Lambda U^{-1}. \tag{A14}$$

Here the diagonal matrix, Λ, is composed of the eigenvalues of A, λ_k:

$$\Lambda_{kl} = \delta_{kl}\lambda_k. \tag{A15}$$

It should be noted that in this paper we do not use the usual convention and do not mean summation for the double indices. It is also interesting to note that each eigenvector corresponds to a wave, while the eigenvalues describe the wave speed.

In the present calculation, Roe's (1981, 1986) approximate Riemann solver was used. This method finds an exact solution to the linearized hydrodynamic equations at the initial discontinuity. This linearized solution is used to construct the approximate U and Λ matrices. In the radial time step operator, L_r, these matrices can be expressed as

$$U = \begin{bmatrix} 1 & 0 & 1 & 1 \\ u_r - a & 0 & u_r & u_r + a \\ u_\Theta & u_\Theta & u_\Theta & u_\Theta \\ h - u_r a & u_\Theta^2 & \frac{1}{2}(u_r^2 + u_\Theta^2) & h + u_r a \end{bmatrix} \tag{A16}$$

$$\Lambda = \begin{bmatrix} u_r - a & 0 & 0 & 0 \\ 0 & u_r & 0 & 0 \\ 0 & 0 & u_r & 0 \\ 0 & 0 & 0 & u_r - a \end{bmatrix}, \tag{A17}$$

where

$$a = \sqrt{\frac{\gamma p}{\rho}} \tag{A18}$$

and

$$h = \frac{a^2}{\gamma - 1} + \frac{1}{2}(u_r^2 + u_\Theta^2). \tag{A19}$$

In the azimuthal time-step operator, L_Θ, the U and Λ matrices become

$$U = \begin{bmatrix} 1 & 0 & 1 & 1 \\ u_r & u_r & u_r & u_r \\ u_\Theta - a & 0 & u_\Theta & u_\Theta + a \\ h - u_\Theta a & u_r^2 & \frac{1}{2}(u_r^2 + u_\Theta^2) & h + u_\Theta a \end{bmatrix} \tag{A20}$$

$$\Lambda = \begin{bmatrix} u_\Theta - a & 0 & 0 & 0 \\ 0 & u_\Theta & 0 & 0 \\ 0 & 0 & u_\Theta & 0 \\ 0 & 0 & 0 & u_\Theta + a \end{bmatrix}. \tag{A21}$$

Next we introduce a modified vector, $\hat{\mathbf{w}}$:

$$\hat{\mathbf{w}} = U^{-1}\mathbf{w}. \tag{A22}$$

The same operator can also be used to define $\hat{\mathbf{d}}$ and $\hat{\mathbf{P}}$. The components of the modified parameter vector satisfy the following equation:

$$\frac{\partial \hat{w}_k}{\partial t} + \lambda_k \frac{\partial \hat{w}_k}{\partial x} = \hat{P}_k. \tag{A23}$$

For positive eigenvalues this equation has the following solution:

$$\hat{w}_k(x, t) = \begin{cases} \overset{Y}{w}_{Lk} + (x - \lambda_k t)\hat{d}_{Lk} + t\hat{P}_{Lk} & x < 0 \\ \hat{w}_{Lk} + (x - \lambda_k t)\hat{d}_{Lk} + t\hat{P}_{Lk} + \dfrac{x}{\lambda_k}(\hat{P}_{Rk} - \hat{P}_{Lk}) & 0 < x < \lambda_k t \\ \hat{w}_{Rk} + (x - \lambda_k t)\hat{d}_{Rk} + t\hat{P}_{Rk} & x > \lambda_k t. \end{cases} \tag{A24}$$

In the case when the eigenvalue is negative the solution becomes

$$\hat{w}_k(x, t) = \begin{cases} \overset{Y}{w}_{Lk} + (x - \lambda_k t)\hat{d}_{Lk} + t\hat{P}_{Lk} & x < \lambda_k t \\ \hat{w}_{Lk} + (x - \lambda_k t)\hat{d}_{Lk} + t\hat{P}_{Lk} + \dfrac{x}{\lambda_k}(\hat{P}_{Rk} - \hat{P}_{Lk}) & 0 > x > \lambda_k t \\ \hat{w}_{Rk} + (x - \lambda_k t)\hat{d}_{Rk} + t\hat{P}_{Rk} & x > 0. \end{cases} \quad \text{(A25)}$$

Thus at $x = 0$ the solution for an arbitrary eigenvalue can be expressed as

$$\hat{w}_k(0, t) = \frac{\lambda_k + |\lambda_k|}{2\lambda_k}(\hat{w}_{Lk} - \lambda_k t\hat{d}_{Lk} + t\hat{P}_{Lk}) + \frac{\lambda_k - |\lambda_k|}{2\lambda_k}(\hat{w}_{Rk} - \lambda_k t\hat{d}_{Rk} + t\hat{P}_{Rk}). \quad \text{(A26)}$$

Now the flux at the discontinuity can be expressed as

$$F_k(0, t) = A\mathbf{w}(0, t) = U\,\Lambda\,U^{-1}\mathbf{w}(0, t) = U\,\Lambda\,\hat{\mathbf{w}} \quad \text{(A27)}$$

or in component notation

$$F_k(0, t) = \sum_l U_{kl}\lambda_l\hat{w}_l(0, t). \quad \text{(A28)}$$

Substituting our previous results, we obtain the following expression for the flux at the discontinuity,

$$\mathbf{F}(0, t) = \frac{1}{2}(\mathbf{F}(\mathbf{w}^+) + \mathbf{F}(\mathbf{w}^-)) - \frac{1}{2}|A|(\mathbf{w}^+ - \mathbf{w}^-), \quad \text{(A29)}$$

where

$$\mathbf{w}^+ = \mathbf{w}_R - tA\mathbf{d}_R + t\mathbf{P}_R \quad \text{(A30)}$$

$$\mathbf{w}^- = \mathbf{w}_L - tA\mathbf{d}_L + t\mathbf{P}_L \quad \text{(A31)}$$

and $|A|$ is the following matrix:

$$|A|_{kl} = \sum_{i,j} U_{ki}|\Lambda_{ij}|U_{jl}^{-1} = \sum_i U_{ki}|\lambda_i|U_{il}^{-1}. \quad \text{(A32)}$$

Let us apply this result to the boundary between cells j and $j + 1$. In this case it is assumed that the slope of gas parameters is linear and constant within one cell. The slope is also considered to be constant during a time step, with its value determined at the middle of the time interval. This means that

$$\mathbf{w}^+ = \mathbf{w}^n_{j+1/2,R} - \frac{\Delta t}{2}A\frac{\mathbf{w}^n_{j+3/2,L} - \mathbf{w}^n_{j+1/2,R}}{\Delta x_{j+1}} + \frac{\Delta t}{2}\mathbf{P}^n_{j+1} \quad \text{(A33)}$$

$$\mathbf{w}^- = \mathbf{w}^n_{j+1/2,L} - \frac{\Delta t}{2}A\frac{\mathbf{w}^n_{j-1/2,R} - \mathbf{w}^n_{j+1/2,L}}{\Delta x_j} + \frac{\Delta t}{2}\mathbf{P}^n_j. \quad \text{(A34)}$$

On the other hand we know that $A\mathbf{w} = \mathbf{F}$, and these equation can be also written as

$$\mathbf{w}^+ = \mathbf{w}^n_{j+1/2,R} - \frac{\Delta t}{2\Delta x_{j+1}}(\mathbf{F}^n_{j+3/2,L} - \mathbf{F}^n_{j+1/2,R}) + \frac{\Delta t}{2}\mathbf{P}^n_{j+1} \quad \text{(A35)}$$

$$\mathbf{w}^- = \mathbf{w}^n_{j+1/2,L} - \frac{\Delta t}{2\Delta x_j}(\mathbf{F}^n_{j-1/2,R} - \mathbf{F}^n_{j+1/2,L}) + \frac{\Delta t}{2}\mathbf{P}^n_j. \quad \text{(A36)}$$

Substituting Eqs. (A7) and (A8) into these relations one obtains

$$\mathbf{w}^+ = \mathbf{w}^{n+1/2}_{j+1} - \frac{1}{2}\Delta x_{j+1}R\left(\frac{\Delta_+\mathbf{w}^n_{j+1}}{\Delta_-\mathbf{w}^n_{j+1}}\right)\frac{\Delta_+\mathbf{w}^n_{j+1} + \Delta_-\mathbf{w}^n_{j+1}}{2} \quad \text{(A37)}$$

$$\mathbf{w}^- = \mathbf{w}^{n+1/2}_j + \frac{1}{2}\Delta x_j R\left(\frac{\Delta_+\mathbf{w}^n_j}{\Delta_-\mathbf{w}^n_j}\right)\frac{\Delta_+\mathbf{w}^n_j + \Delta_-\mathbf{w}^n_j}{2}, \quad \text{(A38)}$$

where the halftime parameter vectors are defined as

$$\mathbf{w}_j^{n+1/2} = \mathbf{w}_j^n - \frac{\Delta t}{2\Delta x_j}(\mathbf{F}_{j+1/2,L}^n - \mathbf{F}_{j-1/2,r}^n) + \frac{\Delta t}{2}\mathbf{P}_j^n. \quad \text{(A39)}$$

Comparing expressions (A37) and (A38) with Eqs. (A7) and (A8) shows that one can interpolate in time by using the same slopes at $t_{n+1/2}$ as at t_n:

$$\mathbf{w}^+ = \mathbf{w}_{j+1/2,R}^{n+1/2} \quad \text{(A40)}$$

$$\mathbf{w}^- = \mathbf{w}_{j+1/2,L}^{n+1/2}. \quad \text{(A41)}$$

In summary, the one-dimensional time step calculation starts with deriving the initial gas parameter values at the right and left sides of the cell boundaries using Eqs. (A7) and (A8). These vectors are used to calculate an intermediate solution for the middle of the time step, given by Eq. (A39). With the help of these half-time values the $\mathbf{w}^+$ and $\mathbf{w}^-$ vectors are obtained by Eqs. (A37) and (A38). Next Roe's modified approximate Riemann solver is applied to determine the U and Λ matrices. These tensors are given by Eqs. (A16) and (A17) for the radial step and by Eqs. (A20) and (A21) for the azimuthal one. The fluxes at the cell boundaries can now be calculated using Eq. (A29). Finally, the cell boundary fluxes are used in Eq. (A6) to calculate the solution at the end of the time step.

ACKNOWLEDGMENTS

The authors are indebted to Dr. Bram van Leer for his advice in developing the second-order Godunov-type numerical scheme to solve the coupled, time-dependent multidimensional partial differential equation system. We are also grateful to Dr J F. Crifo for his valuable comments about the original manuscript. This work was supported by NSF Grant AST-8605994 and NASA Grant NAGW-1366 Acknowledgment is also made to the National Center for Atmospheric Research sponsored by NSF for the computing time used in this research.

REFERENCES

CRIFO, J F 1988 Collisional coma models An unorthodox overview, *Adv. Space Res.*, in press

CRIFO, J. F. 1989 Inferences concerning water vapour viscosity and meant free path at low temperatures, *Astron. Astrophys* , in press

FROMM, J E. 1968. A method for reducing dispersion in convective difference schemes, *J. Comput. Phys* **3,** 176

GOMBOSI, T. I., K. SZEGO, B E GRIBOV, R Z SAGDEEV, V. D SHAPIRO, V. I. SHEVCHENKO, AND T E. CRAVENS 1983 Gas dynamic calculations of dust terminal velocities with realistic dust size distributions In *Cometary Exploration* (T I Gombosi, Ed.) Vol. 1, p 99 KFKI Press, Budapest, Hungary

GOMBOSI, T. I , T. E CRAVENS, A F NAGY 1985. Time-dependent dusty gas dynamical flow near cometary nuclei *Astroph. J.* **293,** 328

GOMBOSI, T I., A F NAGY, AND T. E. CRAVENS 1986 Dust and neutral gas modeling of the inner atmospheres of comets *Rev Geophys.* **24,** 667

GOMBOSI, T. I., AND A KOROSMEZEY 1988a Cometary dusty gas dynamics In *Outstanding Problems in Solar System Plasma Physics* (J Burch and H Waite, Eds.), AGU, Washington, D C , in press

GOMBOSI, T I., AND A KOROSMEZEY 1988b Modeling of the cometary nucleus—coma interface region. *Adv Space Res* , in press

GOURLAY, A R , AND J L MORRIS 1970. On the comparison of multistep formulations of the optimized Lax–Wendroff method for nonlinear hyperbolic systems in two space variables *J. Comp Phys* **5,** 229.

HARTEN, A. 1983 High resolution schemes for hyperbolic conservation laws *J Comput. Phys.* **49,** 357

HARTEN, A., P. D LAX, AND B. VAN LEER 1983 On upstream differencing and Godunov-type schemes for hyperbolic conservation laws *SIAM Rev.* **25,** 35.

HELLMICH, R , AND H U KELLER On the dust production rates of comets. In *Solid Particles in the Solar System* (J Halliday and B A McIntosh, Eds), p 255 Reidel, Hingham, 1980

KELLER, H U , W A DELAMERE, W F HUEBNER, H J REITSEMA, H. U SCHMIDT, F L WHIPPLE, K WILHELM, W CURDT, R KRAMM, N. THOMAS, C. ARPIGNY, R M. BONNET, S CAZES, M CORADINI, C B. COSMOVICI, D W HUGHES, C JAMAR, D MALAISE, K SCHMIDT, W K. H SCHMIDT, AND P SEIGE 1987 Comet P/Halley's nucleus and its activity *Astron Astrophys.* **187,** 807.

KITAMURA, Y 1986. Axisymmetric dusty-gas jet in the inner coma of a comet *Icarus* **66,** 241.

KITAMURA, Y 1987. Axisymmetric dusty-gas jet in the inner coma of a comet II. The case of isolated jets. *Icarus* **72,** 555

MARCONI, M. L , AND D A MENDIS 1982. The photochemical heating of the cometary atmosphere, *Astrophys J* **260,** 386

MARCONI, M L , AND D. A MENDIS 1983 The atmosphere of a dirty cometary nucleus, A two-phase multi-fluid model *Astrophys J* **273,** 381.

MARCONI, M. L., AND D A. MENDIS 1984. The effects of the diffuse radiation fields due to multiple scattering and thermal reradiation by dust on the dynamics and thermodynamics of a dusty cometary atmosphere. *Astrophys. J* **287,** 445.

MARCONI, M. L., AND D. A. MENDIS 1986 IR heating of Comet Halley's atmosphere. *Earth, Moon Planets* **36,** 249

MENDIS, D A , H. L F HOUPIS, AND M. L MARCONI 1985. The physics of comets. *Fundam Cosmic Phys* **10,** 1.

PROBSTEIN, R F 1968. The dusty gas dynamics of comet heads. In *Problems of Hydrodynamics and Continuum Mechanics* Soc. Industr Appl Math , p 568.

ROE, P L. 1981. Approximate Riemann solvers, parameter vectors, and difference schemes *J Comput. Phys.* **43,** 357.

ROE, P. L. 1986. Characteristic-based schemes for the Euler equations, *Annu Rev Fluid Mech* **18,** 337.

SHULMAN, L M 1972. *Dinamika Kometnykh Atmospher—Neutral'nyi Gaz.* Naukova Dumka, Kiev.

VAN ALBADA, G D , B VAN LEER, AND W. W ROBERTS 1982. A comparative study of computional methods in gas dynamics. *Astron. Astrophys* **108,** 76.

VAN LEER, B. 1977 Towards the ultimate conservative difference scheme. IV A new approach to numerical convection *J. Comput Phys.* **23,** 276.

VERGAZOV, M A , AND K V KRASNOBAEV 1985. Axisymmetric flow of reacting gas from a comet nucleus. *Sov Astron. Lett.* **11,** 232.

WHIPPLE, F L. 1950 A comet model I The acceleration of comet Encke *Astrophys J.* **111,** 375